



저작자표시-비영리-변경금지 2.0 대한민국

이용자는 아래의 조건을 따르는 경우에 한하여 자유롭게

- 이 저작물을 복제, 배포, 전송, 전시, 공연 및 방송할 수 있습니다.

다음과 같은 조건을 따라야 합니다:



저작자표시. 귀하는 원저작자를 표시하여야 합니다.



비영리. 귀하는 이 저작물을 영리 목적으로 이용할 수 없습니다.



변경금지. 귀하는 이 저작물을 개작, 변형 또는 가공할 수 없습니다.

- 귀하는, 이 저작물의 재이용이나 배포의 경우, 이 저작물에 적용된 이용허락조건을 명확하게 나타내어야 합니다.
- 저작권자로부터 별도의 허가를 받으면 이러한 조건들은 적용되지 않습니다.

저작권법에 따른 이용자의 권리는 위의 내용에 의하여 영향을 받지 않습니다.

이것은 [이용허락규약\(Legal Code\)](#)을 이해하기 쉽게 요약한 것입니다.

[Disclaimer](#)

공학박사 학위논문

**Sulfur-Doped Graphene and Tin Sulfides
as High Capacity Anode Materials for
Sodium Ion Batteries**

소듐 이온 전지 고용량 음극 물질로서
황도핑된 그래핀과 황화주석에 관한 연구

2018 년 8 월

서울대학교 대학원

화학생물공학부

Aihua Jin

Abstract

Sulfur-Doped Graphene and Tin Sulfides as High Capacity Anode Materials for Sodium Ion Batteries

Aihua Jin

School of Chemical and Biological Engineering

The Graduate School

Seoul National University

Lithium ion batteries (LIBs) have been regarded as the most widely used power sources for many aspects such as portable electronics and electric vehicles, due to the demands for clean energy for the past few decades. However, the lithium resources are limited and non-uniformly distributed globally, so the cost of materials increased by the demands of LIBs. Thus the alternatives should be considered for substituting LIBs.

Among many kinds of batteries, sodium ion batteries (NIBs) have been gaining great attention by the natural abundance and low cost of sodium resources. Na share similar chemical properties with Li, that the fundamental principle of the LIBs and NIBs are identical. The enormous previous researches of LIBs provide great guidance for NIB anode materials. However, it still needs

to explore appropriate anode materials for NIBs. Therefore, a major focus has been to search for high capacity anode materials that will satisfy increasing demands.

The overview of NIBs are introduced in chapter 1 including the benefits of NIBs. In addition, electrode materials currently being investigated as cathode and anode materials in NIBs are also introduced. The structure of the cathode can be divided into three categories while anode, although having a variety of different structures, all generally follow one of three reaction mechanisms.

In chapter 2, the electrochemical properties of heteroatom-doped graphene is discussed. In this chapter the heteroatom-doped graphene with high doping levels and disordered structures were prepared through a simple and economical thermal process. These solvothermal-derived graphene showed excellent performance as an anode material for SIBs. It exhibited a high reversible capacity of 380 mAh g⁻¹ after 300 cycles at 100 mA g⁻¹, excellent rate performance 217 mAh g⁻¹ at 3200 mA g⁻¹ and superior cycling performance at 2.0 A g⁻¹ during 1000 cycles with negligible capacity fade. The main reasons for the excellent cycle performance of SG are likely due to the large interlayer distances, highly disordered structures and greater number of active sites for Na ion storage than others. In addition, by doping with sulfur, as well as lowering the oxygen content, the capacity and cycle performance were significantly enhanced.

In chapter 3, novel tin (II) sulfide/carbon (SnS/C) composites were prepared, through a ball-milling method, as anode materials for sodium ion batteries. Their electrochemical performance has been significantly improved when compared

to bare SnS, especially in cycling stability and rate capabilities. SnS/C composites exhibit excellent capacity retention, at various current rates, and deliver capacities as high as 400 mAh g⁻¹ even at the high current density of 800 mA g⁻¹ (2C). Ex-situ transmission electron microscopy, X-ray diffraction and operando X-ray absorption near edge structure studies have been performed in order to better understand the reaction mechanism of SnS/C composites.

Keywords: sodium ion batteries, anodes, sulfur doped graphene, tin sulfides, reaction mechanism

Student number: 2014-30254

List of Tables

Table 1. 1 Sodium versus lithium characteristics. Adapted from Ref [3]	14
Table 2. 1 Elemental analysis data for S-SG and pristine SG.....	41
Table 2. 2 Electrochemical performances of various carbon-based materials as sodium-ion battery anode materials.....	62

List of Figures

Figure 1. 1 Schematic illustration of the lithium ion batteries. Adapted from Ref [4]	2
Figure 1. 2 Crystalline structures and voltage–composition curves of (a) layered-LiCoO ₂ (R3-m S.G.), (b) spinel–LiMn ₂ O ₄ (Fd-3m S.G.); and (c) olivine–LiFePO ₄ (Pnma S.G.). Adapted from Ref [6].....	5
Figure 1. 3 A schematic representation of the different reaction mechanisms observed in electrode materials for lithium batteries. Black circles: voids in the crystal structure, blue circles: metal, yellow circles: lithium. Adapted from Ref [2].....	8
Figure 1. 4 Specific capacities and capacity densities for selected alloying reactions. Values for graphite are given as a reference. Adapted from Ref [2]	9
Figure 1. 5 Lithium demand and availability and number of electric vehicles (EVs), hybrid electric vehicles (HEVs) and plugin hybrid electric vehicles (PHEVs) over time. In low availability of lithium/optimistic EV/HEV/PHEV production scenarios, lithium could run out in the near future. Adapted from Ref [3]	11
Figure 1. 6 Fluctuation of the price and production of Li ₂ CO ₃ over time. The sharp rise in price in the mid-2000s was caused in part by increases in demand for lithium batteries. Adapted from Ref [3]	12
Figure 1. 7 Schematic illustration of the sodium ion batteries.	13
Figure 1. 8 Recent research progress in sodium ion batteries of anode. Adapted from Ref [27]	16
Figure 1. 9 Crystal structures of various Na _x MO _y : (a) P2-Na _x CoO ₂ , (b) O3-Na _x CoO ₂ , (c) P3-Na _x CoO ₂ (Na: yellow, Co: blue, O: red). Adapted from Ref [26]	17
Figure 1. 10 Recent research progress in sodium ion batteries of cathode. Adapted from Ref [27]	21
Figure 1. 11 Schematic illustration of sodium storage in graphite-based materials.	

Adapted from Ref [42]	22
Figure 1. 12 Schematic diagram illustrating the phase transition process between SnS ₂ and SnS. The crystal structures of hexagonal SnS ₂ (a, b, c) and orthorhombic SnS (d, e, f) are shown in different sectional views. Adapted from Ref [49].....	23
Figure 1. 13 Theoretical equilibrium redox potentials of (A) Na–Si, (B) Na–Ge, (C) Na–Sn, and (D) Na–Pb. Adapted from Ref [17]	24
Figure 1. 14 (a-c) Three <i>a</i> -Na _x Sn phases in the single-phase sodiation. (d) Schematic illustration of the structural evolution of Sn nanoparticles during the sodiation. Adapted from Ref [50]	25
Figure 2. 1 Scheme of synthesis illustration of S-SG and A photographic image of DMSO and S-SG.....	37
Figure 2. 2 SEM images of S-SG and SG.	38
Figure 2. 3 (a) TEM and (b) high-resolution TEM images of S-SG.	39
Figure 2. 4 (a) TEM and (b) high-resolution TEM images of pristine SG.	40
Figure 2. 5 TEM image and EDS elemental mapping of S-SG.....	42
Figure 2. 6 S-SG and pristine SG XPS spectra of (a)XPS survey spectra, (b) high resolution S2p with S2p _{3/2} , S2p _{1/2} , and oxidized sulfur, and (c) high resolution C1s spectra.....	45
Figure 2. 7 Raman spectrum of S-SG and pristine SG.....	46
Figure 2. 8 XRD patterns of S-SG and pristine SG.....	47
Figure 2. 9 The TEM images (a) S-SG and (c) pristine SG, and (b, d) corresponding SAED patterns, respectively.	48
Figure 2. 10 (a) Nitrogen-adsorption/desorption isotherms of S-SG and pristine SG. (b) BJH pore size distributions of S-SG and pristine SG as calculated from the adsorption isotherms.	49
Figure 2. 11 Voltage profiles of (a) S-SG and (b) pristine SG at a current density of 100 mA g ⁻¹ . Cyclic voltammograms of (c) S-SG and (d) pristine SG at a scan rate of 0.1 mV s ⁻¹	52
Figure 2. 12 Cycle performance of pristine SG and S-SG at current densities of 100 and 200 mA g ⁻¹	53

Figure 2. 13 Cycle performance of S-SG and pristine SG at a current density of 500 mA g ⁻¹	55
Figure 2. 14 Rate performance of pristine SG and S-SG at different current densities.....	56
Figure 2. 15 The voltage profiles of S-SG at a current density of (a) 100 mAh g ⁻¹ (red: from constant current cycling, blue: from stepwise current cycling) and (b) 200 mAh g ⁻¹ (red: from constant current cycling, blue: from stepwise current cycling); the differential capacity plots of S-SG at a current density of (c) 100 mAh g ⁻¹ (red: from constant current cycling, blue: from stepwise current cycling) and (d) 200 mAh g ⁻¹ (red: from constant current cycling, blue: from stepwise current cycling).	59
Figure 2. 16 The differential capacity plots of S-SG at a current density of 50 mAh g ⁻¹	60
Figure 2. 17 Cycle performance of S-SG at a current density of 2.0 A g ⁻¹	61
Figure 2. 18 Electrochemical impedance spectrum for S-SG and pristine SG (a) before cycling, and (b) after 1 cycle.....	63
Figure 3. 1 XRD patterns of (a) bare SnS and SnS/C nanocomposites (top) and SnS from JCPDS No. 14-0620 (bottom). (b) Crystal structure of SnS along the [001] direction (<i>c</i> -axis direction).....	73
Figure 3. 2 Schematic illustration of morphology of (a) bare SnS and (b) SnS/C nanocomposites.	74
Figure 3. 3 XANES spectra of SnS/C nanocomposites (blue line), commercial SnS (red dots) and SnS ₂ (green dash).....	75
Figure 3. 4 SEM images of (a-b) bare SnS, (c-d) SnS/C nanocomposites.	77
Figure 3. 5 TEM images of (a-b) bare SnS (inset of c shows fast Fourier transform (FFT) image of whole region in c.), (c-d) SnS/C nanocomposites.	78
Figure 3. 6 (a)-(d) High-resolution TEM images of SnS/C nanocomposites, and (e) inverse fast Fourier transformed (FFT) image from the region circled by red in inset. Inset shows FFT image of (d).	79
Figure 3. 7 STEM image of SnS/C nanocomposites.....	80

Figure 3. 8 Voltage profiles of (a) bare SnS and (b) SnS/C nanocomposites at a current density of 100 mA g ⁻¹	81
Figure 3. 9 Cyclic voltammograms of (a) bare SnS and (b) SnS/C nanocomposites at a scan rate of 0.1 mV s ⁻¹	82
Figure 3. 10 Cyclic voltammograms of SnS/C nanocomposites at a scan rate of 0.1 mV s ⁻¹ with different cut off voltage ranges.	83
Figure 3. 11 Cycle performance of bare SnS and SnS/C nanocomposites at a current density of 100 mA g ⁻¹	85
Figure 3. 12 Rate properties of bare SnS and SnS/C nanocomposites at various current densities.	86
Figure 3. 13 Voltage profiles of (b) bare SnS and (c) SnS/C nanocomposites at various current densities.	90
Figure 3. 14 Cycle performance of 2D SnS/C nanocomposites at various current densities.	91
Figure 3. 15 (a) XRD patterns of tin sulfide/mesoporous carbon (CMK) composites prepared by ball milling method. (b) Voltage profiles of tin sulfide/mesoporous carbon (CMK) composites at a current density of 100 mA g ⁻¹	92
Figure 3. 16 (a) Rate properties of tin sulfide/mesoporous carbon (CMK) composites. (b) Cycle performance of tin sulfide/mesoporous carbon (CMK) composites at various current densities.	93
Figure 3. 17 <i>Ex-situ</i> XRD patterns during the first sodiation and desodiation process.	94
Figure 3. 18 (a) <i>operando</i> XANES spectra of SnS/C nanocomposites at Sn K edge during the first sodiation and desodiation process.	95
Figure 3. 19 (a) TEM image and (b) SAED pattern of SnS/C nanocomposites at fully sodiated state (0.01 V). (c) TEM image and (d) SAED pattern of SnS/C nanocomposites at fully desodiated state (3.0 V).	96
Figure 3. 20 XANES spectra of SnS/C nanocomposites at Sn K edge composites before battery test, after the first and second sodiation and desodiation.	97

Contents

Abstract	i
List of Tables	iv
List of Figures	v
Chapter 1. Introduction	1
1.1 Lithium ion batteries	1
1.1.1 General introduction	1
1.1.3 Anode materials in lithium ion batteries	4
1.2.1 General introduction	10
1.2.2 Cathode materials in sodium ion battery	15
1.2.3 Anode materials in sodium ion battery	18
Chapter 2. Solvothermal-Derived S-doped Graphene as an Anode Material for Sodium-Ion Batteries	31
2.1. Introduction	31
2.2. Experimental section	33
2.2.1. Reagents	33
2.2.2. Synthesis method of S-SG	33
2.2.3. Synthesis method of pristine SG	34
2.2.4. Materials characterization	34
2.2.5 Electrochemical characterization of materials	35
2.3.2 Electrochemical performance of of S-SG and SG	50
2.4. Conclusions	64
2.5. References	65
Chapter 3. SnS/C Nanocomposites as Sodium Ion Battery Anode Materials with high Capacity and superior Rate Capability	68
3.1 Introduction	68

3.2. Experimental section	70
3.2.1 Preparation method of tin (II) sulfide/carbon composites	70
3.2.2 Materials characterization	70
3.2.3 Electrochemical Characterization	70
3.3 Results and discussion	72
3.3.1 Materials characterization of bare SnS and SnS/C nanocomposites	72
3.3.2 Electrochemical properties of bare SnS and SnS/C nanocomposites	76
3.3.3 Reaction mechanism of bare SnS and SnS/C nanocomposites ..	88
3.4 Conclusions	98
3.5 References	99
국문 초록 (Abstract in Korean)	103

Chapter 1. Introduction

1.1 Lithium ion batteries

1.1.1 General introduction

Lithium ion batteries (LIBs) have attracted numerous attention as dominant power source for portable electronics due to the commercialization of LIB by SONY in 1991. [1-3] LIBs have some advantages for these application for the reasons of strong stability, high energy and high power density, long cycle life, high operating voltage and wide range of operating temperature. Therefore LIB have been considered as one of the most promising candidates for hybrid electric vehicles (HEVs), plug-in hybrid electric vehicles (PHEVs), electric vehicles (EVs) and electrical energy storage systems (EES).

As illustrated in Figure 1.1, the operating principle of LIBs. Typical LIBs consist of cathode and anode separated by separator and electrolyte. [4, 5] Separator, which made by a porous polymer material with insulating characteristics, acts as a barrier to prevent the contact between cathode and anode and prevents short circuit. Commonly used electrolyte works as ionic conductor to transport lithium ions to cathode and anode. Electrolytes usually composed of lithium contained salts and solvents. For solvents in LIBs, cycling carbonate and linear carbonate are used with mixture to control the dielectric constant and viscosity. Nowadays, LiCoO_2 and graphite are popularly used in commercial LIBs. During charge process, the Li ions are extracted from cathode material, pass through the electrolyte and finally intercalate to anode materials. The

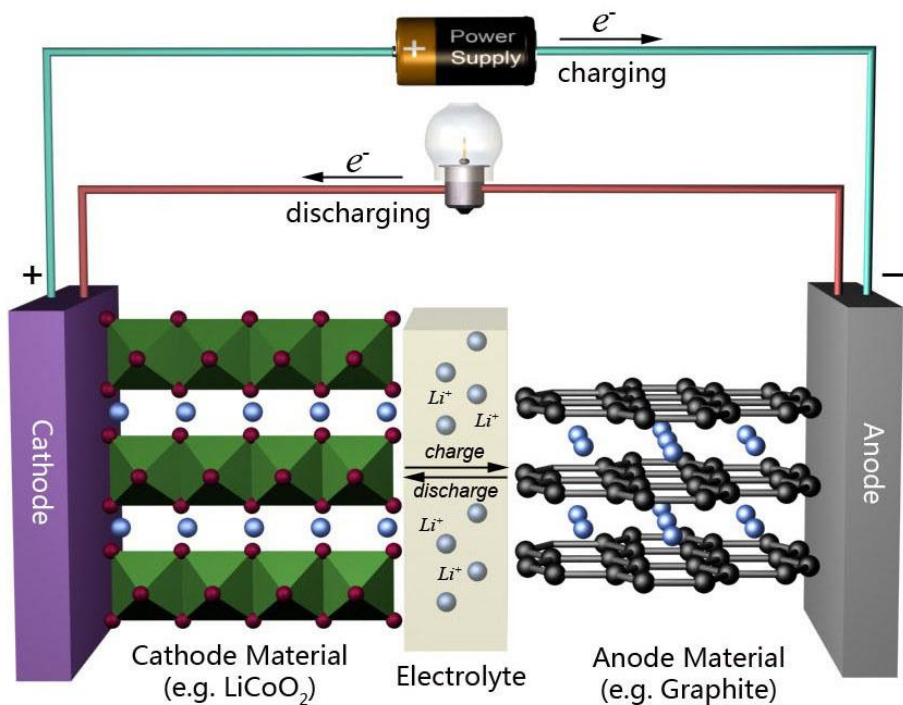


Figure 1. 1 Schematic illustration of the lithium ion batteries. Adapted from Ref [4] (R. Liu, J. Duay, S.B. Lee, *Chemical Communications*, 47 (2011) 1384-1404).

electrons are simultaneously transferred from cathode to anode through external circuit. The reversal reaction occurs during the discharge process. The overall reactions can be expressed as following reaction.



1.1.2 Cathode materials in lithium ion batteries

Generally, cathode materials should have high lithiation and delithiation potential in the aspect of power and energy density. However, high operating cathode materials have been restricted by the electrochemical window of electrolyte. The cathode materials being used recently can be classified into three types as shown in Figure 1.2. [2, 6, 7]

LiCoO₂ has been one of the most popular cathode materials in commercial LIB market owing to its good cycle stability, superior reversibility and moderate high operating potential (Figure 1.2a). The operation voltage of LiCoO₂ is restricted to 4.2 V vs. Li⁺/Li with capacity of 140 mAh g⁻¹, although the theoretical capacity of LiCoO₂ is 274 mAh g⁻¹. When more than half of Li ions are extracted, the phase transition could be occurred and resulted in capacity fading by structural instability. Additionally, the price of cobalt materials are expensive and toxic. Hence, many efforts have been made to fully or partially substitute cobalt to other transition metals, such as LiNiO₂ and LinMnO₂.

LiMn₂O₄ with spinel structure is one of the most conventional cathode materials for the sake of its low cost, low toxic, good structural stability, and high

power capability due to 3D framework. As depicted in Figure 1.2b, LiMn_2O_4 has two step reactions at about 4.0 and 3.0 V. [8] The plateau at 3.0 V can lead to capacity decrease, which closely related to the asymmetric lattice expansion/contraction of electrodes during discharge/charge. This is mainly originated from Jahn-Teller distortion of Mn^{3+} ion and finally resulted in the electrolyte and phase dissolution. [9] To solve this problem, many transition metal ions are used to substitute with Mn ions. Among them, many researches have been focused on $\text{LiNi}_{0.5}\text{Mn}_{0.5}\text{O}_4$ because of its high capacity and high operating voltage. [10, 11]

Olivine LiFePO_4 is one of the most attractive cathode materials owing to its environmentally benignity, low cost, low toxic, high stability, and high thermal stability (Figure 1.2c). LiFePO_4 has a high practical capacity of 165 mAh g^{-1} at operation low potential of 3.4 V vs. Li^+/Li . Thus the energy density and rate capability of LiFePO_4 are relatively low owing to the one dimensional ionic channel and poor electron conductivity. [11]

1.1.3 Anode materials in lithium ion batteries

Three different reaction mechanism of anode materials are shown in Figure 1.3. [2]As anode material, lithium metal has extremely high gravimetric and volumetric capacities (3860 mAh g^{-1} and 2062 mAh cm^{-3} , respectively) and low redox potential. However, the poor cycle stability and safety problem has restricted the commercialization of lithium metal as anode material in lithium secondary batteries. So graphite has firstly used as anode material in LIBs by

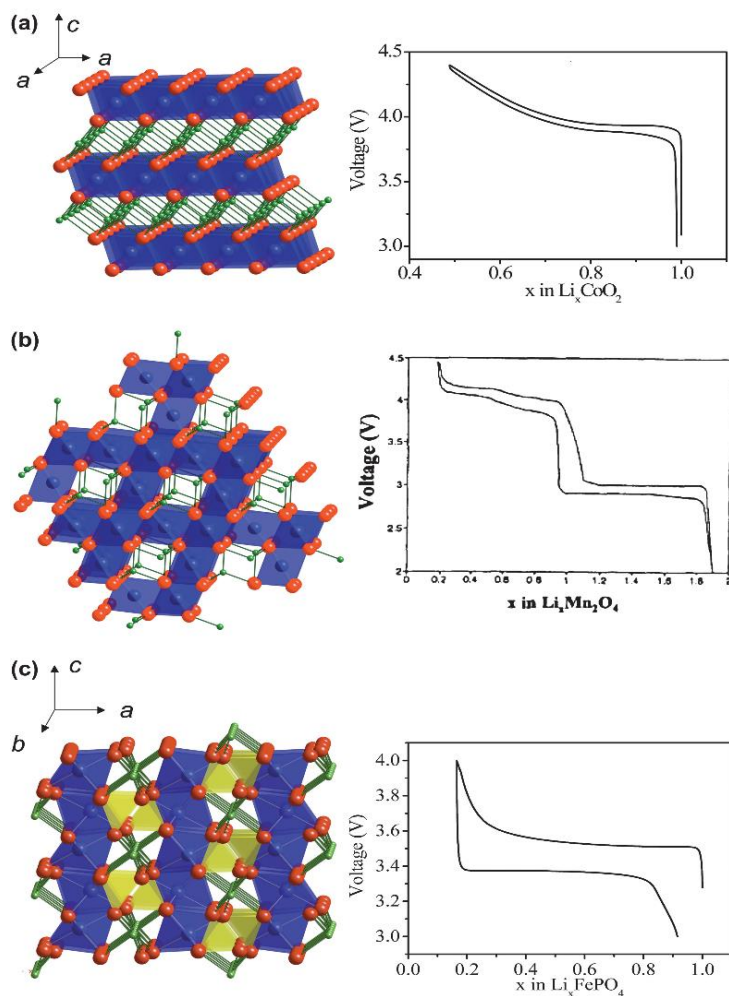
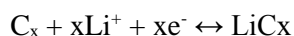


Figure 1. 2 Crystalline structures and voltage–composition curves of (a) layered-LiCoO₂ (R3-m S.G.)—oxygen (red) layers are stacked in ABC sequence, with lithium (green) and cobalt (blue) residing in the octahedral sites of the alternating layers; (b) spinel-LiMn₂O₄ (Fd-3m S.G.)—lithium (green) resides in the tetrahedral sites formed by oxygen stacking; and (c) olivine-LiFePO₄ (Pnma S.G.)—phosphor (yellow) and oxygen form tetrahedral units linking planes of corner-sharing FeO₆ octahedra. Adapted from Ref [6] (Y.S. Meng, M.E. Arroyo-de Dompablo, Energy & Environmental Science, 2 (2009) 589-609).

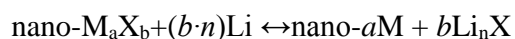
reversible intercalation upon discharging and deintercalation upon charging as following reaction.



The operating potential of graphite is 0.1-0.2 V vs. Li^+/Li with insertion mechanism, which is a little higher than lithium metal. This is important to show high power density. $Li_4Ti_5O_{12}$ is one of the most typical insertion materials in anodes. $Li_4Ti_5O_{12}$ exhibit excellent cyclic stability owing to its almost zero strain during charge/discharge.

Anode materials that undergo alloying reaction generally deliver high gravimetric and volumetric capacities as shown in Figure 1.4, such as Sn, Sb, Si and Ge metals. But they usually suffer from extremely high volume expansion problem during charge and discharge, which finally can cause the pulverization and cracks of active materials with capacity fading. Silicon has the highest theoretical gravimetric capacities in numerous anode materials. However, the main drawback is the huge volume expansion up to 300 % which can lead to rapid capacity fading. Thus, many researches have been introduced, for example, morphology control and nanocomposites. [12, 13]

Conversion reactions are the reaction between lithium and binary M-X compounds (M is transition metal, X can be O, N, F, S, P), which to produce nanoscale metal clusters (2-5 nm) dispersed in a Li_nX matrix as following reaction.



Where n is formal oxidation state of X. [14] Most conversion reaction-based have

higher theoretical capacities than graphite (372 mAh g^{-1}). Even though have such high theoretical capacity, they should be further optimized to overcome the large overpotential and hysteresis. [15] There are much advances on the development of nanostructured materials to solve these drawbacks of conversion reaction-based materials.

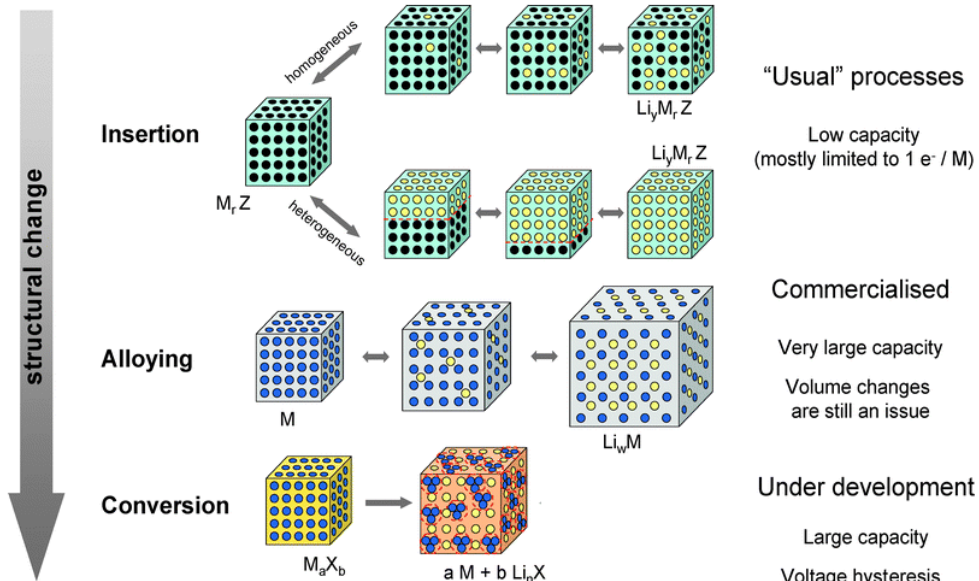


Figure 1. 3 A schematic representation of the different reaction mechanisms observed in electrode materials for lithium batteries. Black circles: voids in the crystal structure, blue circles: metal, yellow circles: lithium. Adapted from Ref [2] (M.R. Palacin, Chemical Society Reviews, 38 (2009) 2565-2575).

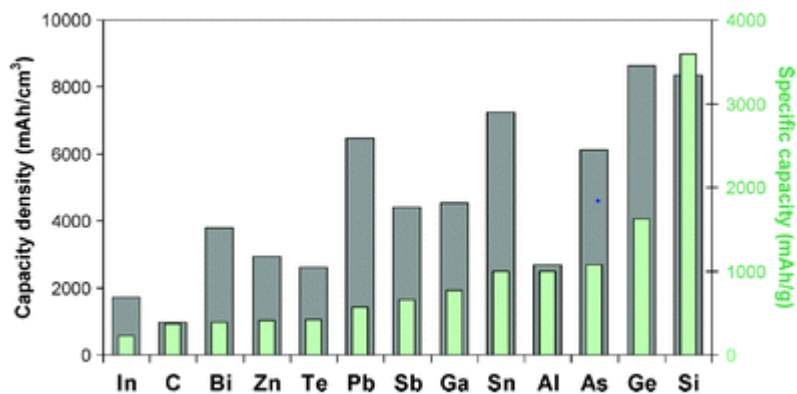


Figure 1. 4 Specific capacities and capacity densities for selected alloying reactions. Values for graphite are given as a reference. Adapted from Ref [2] (M.R. Palacin, Chemical Society Reviews, 38 (2009) 2565-2575).

1.2 Sodium ion batteries

1.2.1 General introduction

In recent years, the applications of LIBs has expanded from portable electronics (e.g., laptop, cellular phone) to large scale applications such as hybrid electric vehicles (HEVs), plug-in hybrid electric vehicles (PHEVs), electric vehicles (EVs), and electrical energy storage systems (EES). [2, 4] However, the geographically constrained Li resources are not sufficient to satisfy the increasing demands of LIBs (Figure 1.5). In addition, the fluctuation of raw material price and production cost are other concerns as shown in Figure 1.6. [16, 17] Therefore, the alternatives should be considered for substituting LIBs. Among many kinds of batteries, sodium ion batteries (NIBs) have been gaining great attention by the natural abundance and low cost of sodium resources. [2, 18]

Li and Na share similar chemical properties, so that the fundamental principle of the LIBs and NIBs are identical. NIBs are also composed of cathode and anode separated with separator (Figure 1.7). [19-22] Thus similar characterization method and intercalation/alloying/conversion chemistry could be applied to the development of NIBs. However, there are some difference between LIBs and NIBs as shown in Table 1.1. [16] Especially, the ionic radius of sodium ion 55% larger than lithium, so the reduction potential of NIBs are ~0.3 V higher than LIBs. Since NIBs are emerging to discover adequate electrode materials for commercialization which exhibit high performance. [23, 24]

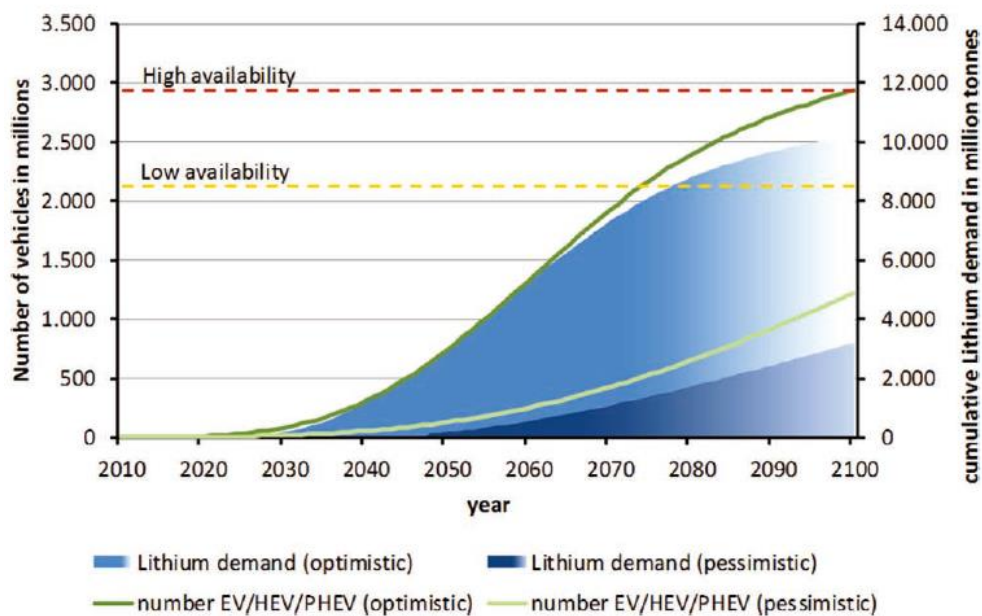


Figure 1. 5 Lithium demand and availability and number of electric vehicles (EVs), hybrid electric vehicles (HEVs) and plugin hybrid electric vehicles (PHEVs) over time. In low availability of lithium/optimistic EV/HEV/PHEV production scenarios, lithium could run out in the near future. Adapted from Ref [3] (M.D. Slater, D. Kim, E. Lee, C.S. Johnson, *Advanced Functional Materials*, 23 (2013) 947-958).

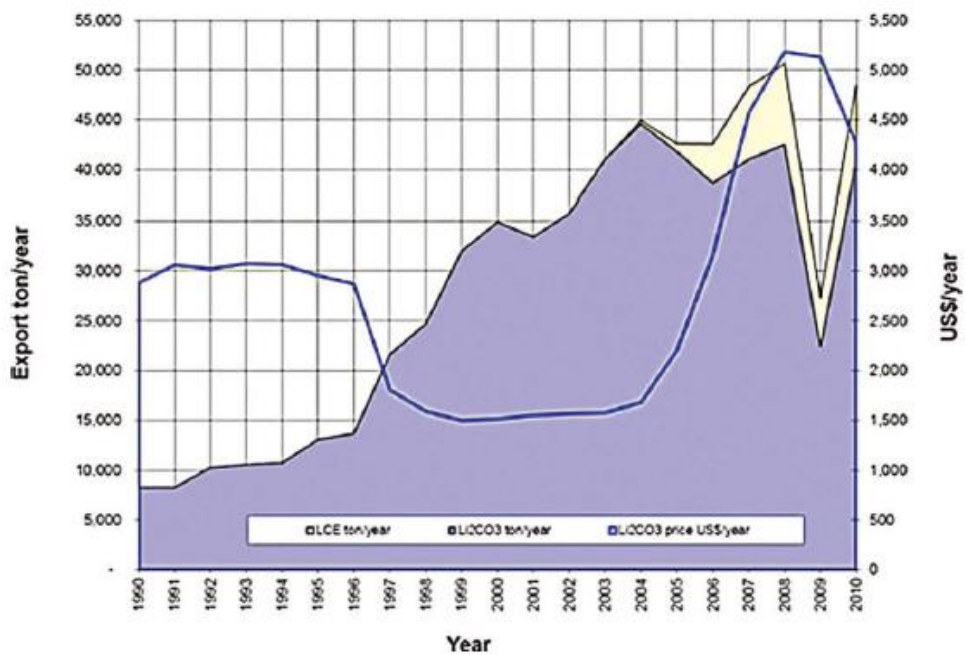


Figure 1. 6 Fluctuation of the price and production of Li_2CO_3 over time. The sharp rise in price in the mid-2000s was caused in part by increases in demand for lithium batteries. Adapted from Ref [3] (M.D. Slater, D. Kim, E. Lee, C.S. Johnson, *Advanced Functional Materials*, 23 (2013) 947-958).

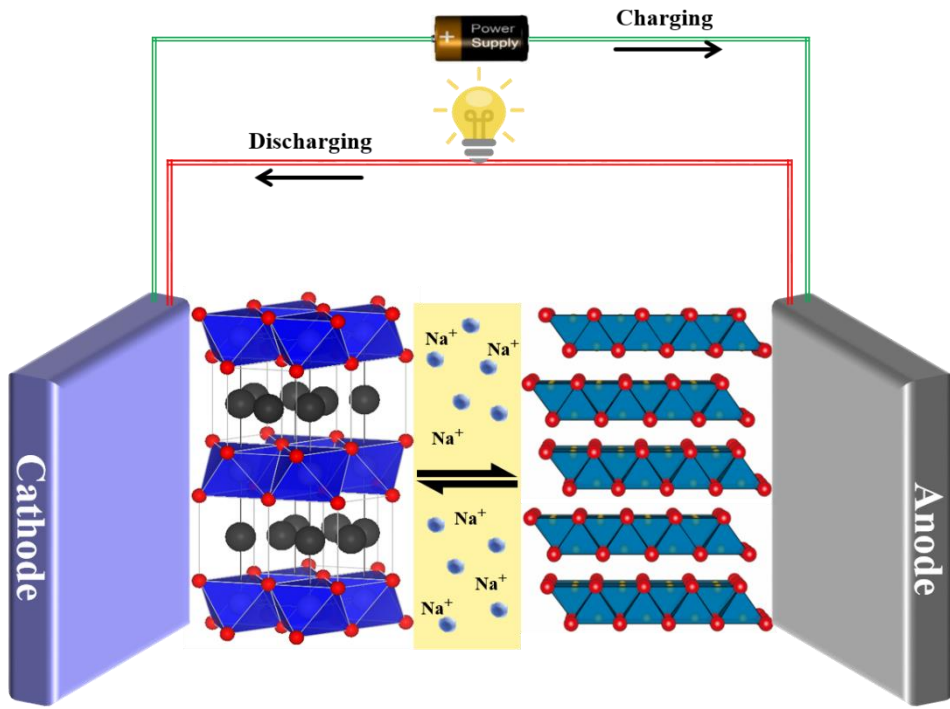


Figure 1. 7 Schematic illustration of the sodium ion batteries.

Table 1.1 Sodium versus lithium characteristics. Adapted from Ref [3] (M.D. Slater, D. Kim, E. Lee, C.S. Johnson, *Advanced Functional Materials*, 23 (2013) 947-958).

Lithium	Sodium	Category
0.76	1.06	Cation radius (Å)
6.9 g mol ⁻¹	23 g mol ⁻¹	Atomic weight
0	0.3 V	E° (vs. Li/Li ⁺)
\$5000/ton	\$150/ton	Cost, carbonates
3829	1165	Capacity (mAh g ⁻¹), metal
Octahedral and tetrahedral	Octahedral and prismatic	Coordination preference

1.2.2 Cathode materials in sodium ion battery

Layered LiMO_2 have been extensively researched as cathode materials in LIBs. Hence, similar NaMO_2 (Co, Ni, Fe, Cr) compounds are also investigated as NIBs cathode. In 1981, Delmas et al. compared the electrochemical properties of various P2- Na_xCoO_2 and O3- Na_xCoO_2 structures as intercalation hosts of Na ions. [25, 26] Various crystal structure of Na_xCoO_2 compounds are performed in Figure 1.8. Among those Na_xCoO_2 , P2- $\text{Na}_{0.7}\text{CoO}_2$ exhibited the highest energy density ($\sim 260 \text{ Wh kg}^{-1}$) in NIB. P2- Na_xMnO_2 shows an electrochemical activity in the Na composition of $0.45 \leq x \leq 0.85$, which is similar to the case of P2- Na_xCoO_2 . However, they revealed poor structural reversibility and a low Na diffusion rate owing to the Jahn-Teller effect of Mn^{3+} dissolution. [27] Therefore, mixed layered metal oxides were adopted to improve the reversibility of P2- Na_xMnO_2 during charge/discharge, such as $\text{Na}_{0.83}[\text{Li}_{0.25}\text{Mn}_{0.75}]\text{O}_2$, $\text{Na}_{0.67}\text{Mg}_{0.2}\text{Mn}_{0.8}\text{O}_2$, $\text{Na}_{0.67}[\text{Mg}_{0.28}\text{Mn}_{0.72}]\text{O}_2$, $\text{Na}_{0.67}\text{Ni}_{0.25}\text{Mg}_{0.1}\text{Mn}_{0.65}\text{O}_2$, and $\text{Na}_{0.67}\text{Cu}_{0.14}\text{Mn}_{0.86}\text{O}_2$. [28-32]

Polyanionic compounds also have been investigated at NIB cathode materials due to their structural diversity and stability. However, they performed relatively low gravimetric capacity because of the presence of heavy polyanion groups such as $(\text{PO}_4)^{3-}$, $(\text{SO}_4)^{2-}$, $(\text{SiO}_4)^{4-}$, and $(\text{P}_2\text{O}_7)^{4-}$. [27] Even though olivine NaFePO_4 has a high theoretical capacity of 154 mAh g^{-1} as NIB cathodes, they cannot be directly used as olivine phase. [33, 34] The maricite NaFePO_4 phase can achieve a reversible capacity of $\sim 142 \text{ mAh g}^{-1}$ and promising rate performance instead of olivine NaFePO_4 .

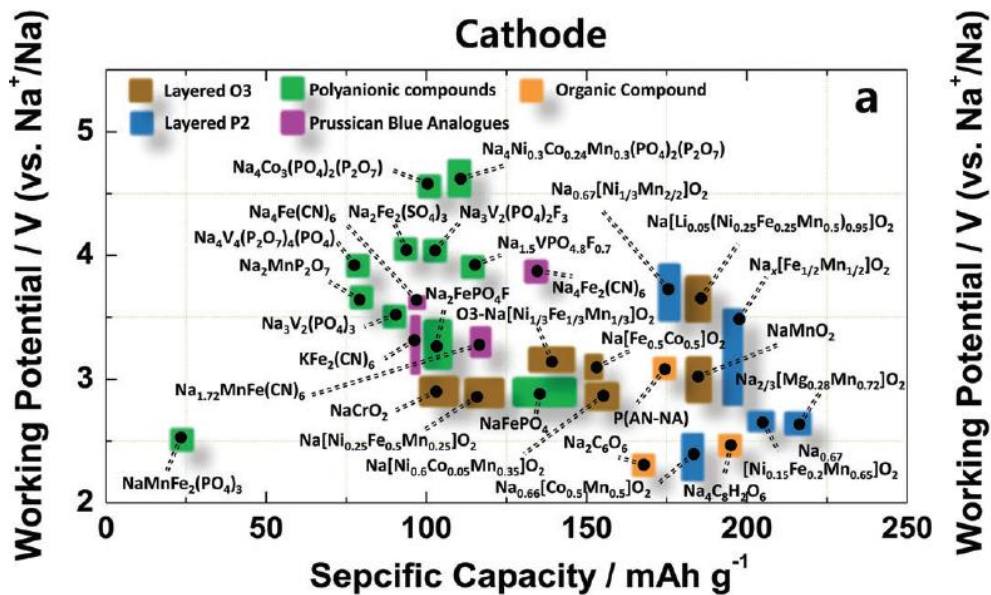


Figure 1. 8 Recent research progress in sodium ion batteries of anode. Adapted from Ref [27] (H. Kim, H. Kim, Z. Ding, M.H. Lee, K. Lim, G. Yoon, K. Kang, *Advanced Energy Materials*, 6 (2016)).

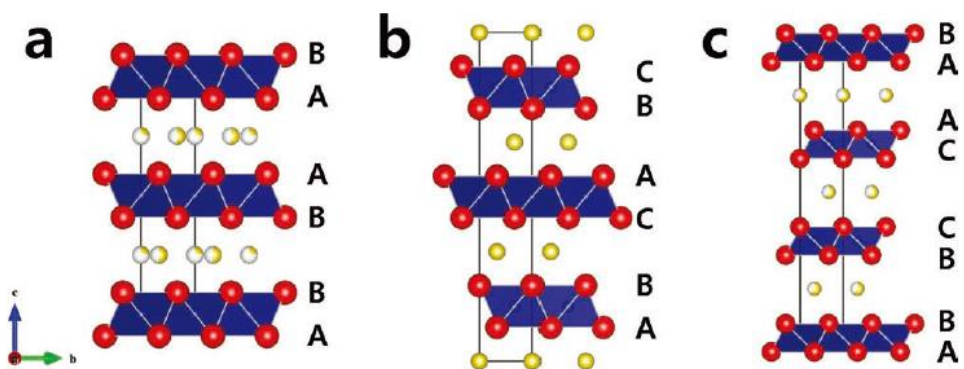


Figure 1. 9 Crystal structures of various Na_xMO_y : (a) P2- Na_xCoO_2 , (b) O3- Na_xCoO_2 , (c) P3- Na_xCoO_2 (Na: yellow, Co: blue, O: red). Adapted from Ref [26] (S.W. Kim, D.H. Seo, X. Ma, G. Ceder, K. Kang, *Advanced Energy Materials*, 2 (2012) 710-721).

In recent years, prussian blue analogues (PBAs) have been used as alternative NIB cathode materials to the layered and polyanionic compounds. [24, 27] Owing to the large alkali ion channels can enable the fast ion transfer during sodiation/desodiation without lattice distortion. $\text{NaFe}_2(\text{CN})_6$ were investigated as cathodes for NIBs and showed a reversible capacity of 118 mAh g^{-1} . [35] Except this, other types of PBAs including $\text{Na}_{1.61}\text{Zn}_3[\text{Fe}(\text{CN})_6]_2 \cdot 3\text{H}_2\text{O}$, $\text{Na}_4\text{Fe}(\text{CN})_6$, and $\text{Na}_{1.96}\text{Mn}[\text{Mn}(\text{CN})_6]_{0.99} \cdot 2\text{H}_2\text{O}$ were also reported as NIB cathodes. [36-38]

1.2.3 Anode materials in sodium ion battery

The enormous previous researches of LIBs provide great guidance for NIB suitable anode materials in the past three decades. However, it still needs to explore appropriate anode materials for NIBs. The recent research progress are presented in Figure 1.10. [18, 24, 27]

Among various anode materials, the carbonaceous materials have been mostly investigated due to the abundant resource, low cost and stability. Regrettably, graphite, the commonly used anode material in LIBs, is proven to be not suitable as NIBs. The main reason is that graphite is electrochemically irreversible so exhibit quite low capacity in NIBs. [39, 40] Y. Wen et al. reported that expanded graphite with interlayer lattice distance of 4.3\AA were prepared by oxidation and partial reduction on graphite. The expanded graphite could show 284 mAh g^{-1} at a current density of 20 mA g^{-1} by enlarging the interlayer lattice distance as shown in Figure 1.11. [41] H. Kim et al. used natural graphite by using ether-based electrolyte instead of carbonate-based. [42] Natural

graphite delivers about 150 mAh g⁻¹ during 2500 cycles, because partial pseudocapacitive behaviors occurs combined with Na⁺-solvent co-intercalation by using ether-based electrolyte. Furthermore, heteroatom doping (e.g., S, F and N) strategy are also used to tune the chemical and physical properties of carbonaceous materials, as it can modulate electronic properties by producing defects and porosities, as well as increase the interlayer distance of carbon. [43-45]

Transition metal oxides and sulfides with various oxidation states can be reversibly sodiation and desodiation either by insertion or conversion such as Fe, Co, Ni, Mo and Sn. Spinel NiCo₂O₄ was firstly published as conversion based anode material in NIBs with a reversible capacity of close to 200 mAh g⁻¹. [46] When compared related metal oxides to metal sulfides, they display improved mechanical stability due to their higher first cycle efficiency and smaller volume change. In addition, Na₂S, the product of sodiation process affords better conductivity than Na₂O from metal oxides. The metal sulfides bond between metal and sulfur is much weaker than the bond in metal oxides, which could be kinetically favorable for conversion reactions. Since, they attracted tremendous attention to focus on the development metal sulfides. [47, 48] Structural phase transition occurred from hexagonal SnS₂ to orthorhombic SnS without adding any additional elements. (Figure 1.12) Both of them were used as NIB anode materials and they exhibited high reversible capacity, especially for SnS. [49]

To substitute the low specific capacity of carbonaceous materials, alloying reaction based materials have been widely studied also in NIBs because of the

high theoretical capacity. Unfortunately, Silicon, which has the highest theoretical capacity in LIBs, could not use in NIBs according to the Na-Si phase diagram (Figure 1.13). Additionally, the theoretical redox potential of Na-Si is close to 0 V vs. Na^+/Na and this is lower than that of Li-Si (ca. 0.3 V vs. Li^+/Li), so that large polarization can be caused by the reason of Na ions inhabitation.

[16, 17] The microstructural changes and phase transformations of Sn nanoparticles were studied during sodiation with in situ TEM. [50] Sn nanoparticles were insertion via a two-phase mechanism with a migrating phase boundary to form amorphous Na_xSn alloy ($X \sim 0.5$) and finally to the crystallized $\text{Na}_{15}\text{Sn}_4$ through a single-phase mechanism as shown in Figure 1.14. Elemental phosphorus (P) is an attractive anode material due to the highest theoretical capacity of 2596 mAh g^{-1} in NIBs. [51, 52] This is several times higher than Sn ($\text{Na}_{15}\text{Sn}_4$, 847 mAh g^{-1}), Pb ($\text{Na}_{15}\text{Pb}_4$, 485 mAh g^{-1}), and Sb (660 mAh g^{-1}). [53-55] J. Qian et al. firstly reported amorphous phosphorus/carbon nanocomposites as sodium ion battery anode materials. [56] They simply prepared amorphous phosphorus/carbon nanocomposites by high energy ball-milling method and it delivered and showed 1764 mAh g^{-1} over 100 cycles. The other alloy based materials also investigated widely.

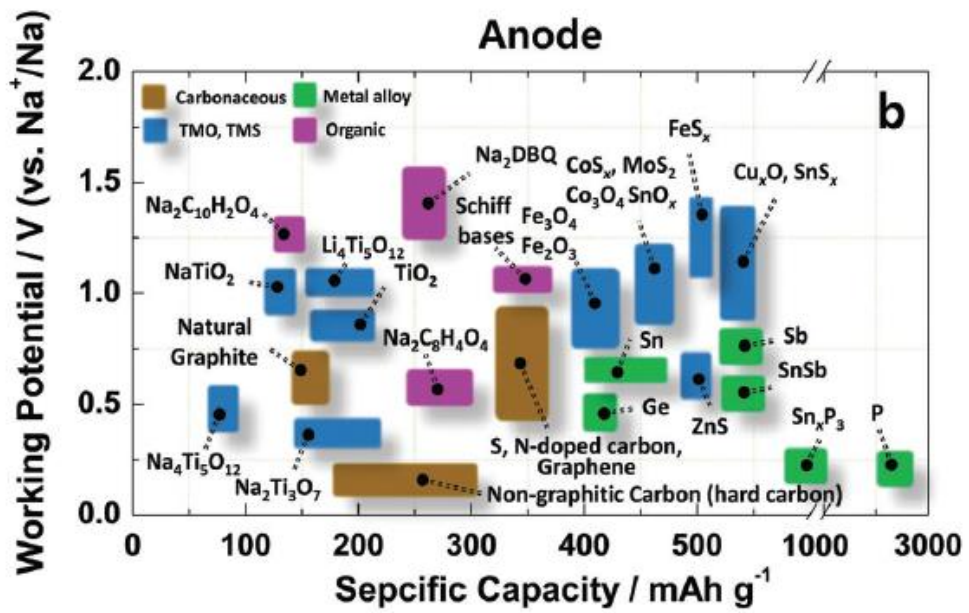


Figure 1. 10 Recent research progress in sodium ion batteries of cathode. Adapted from Ref [27] (H. Kim, H. Kim, Z. Ding, M.H. Lee, K. Lim, G. Yoon, K. Kang, *Advanced Energy Materials*, 6 (2016)).

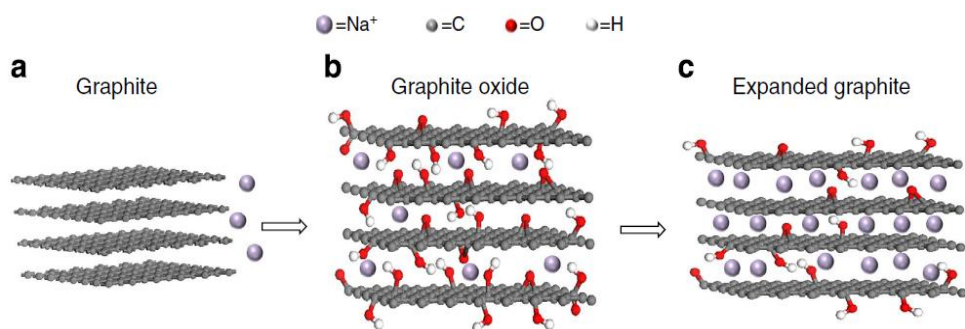


Figure 1. 11 Schematic illustration of sodium storage in graphite-based materials.

Adapted from Ref [42] (Y. Wen, K. He, Y. Zhu, F. Han, Y. Xu, I. Matsuda, Y.

Ishii, J. Cumings, C. Wang, Nature communications, 5 (2014) 4033).

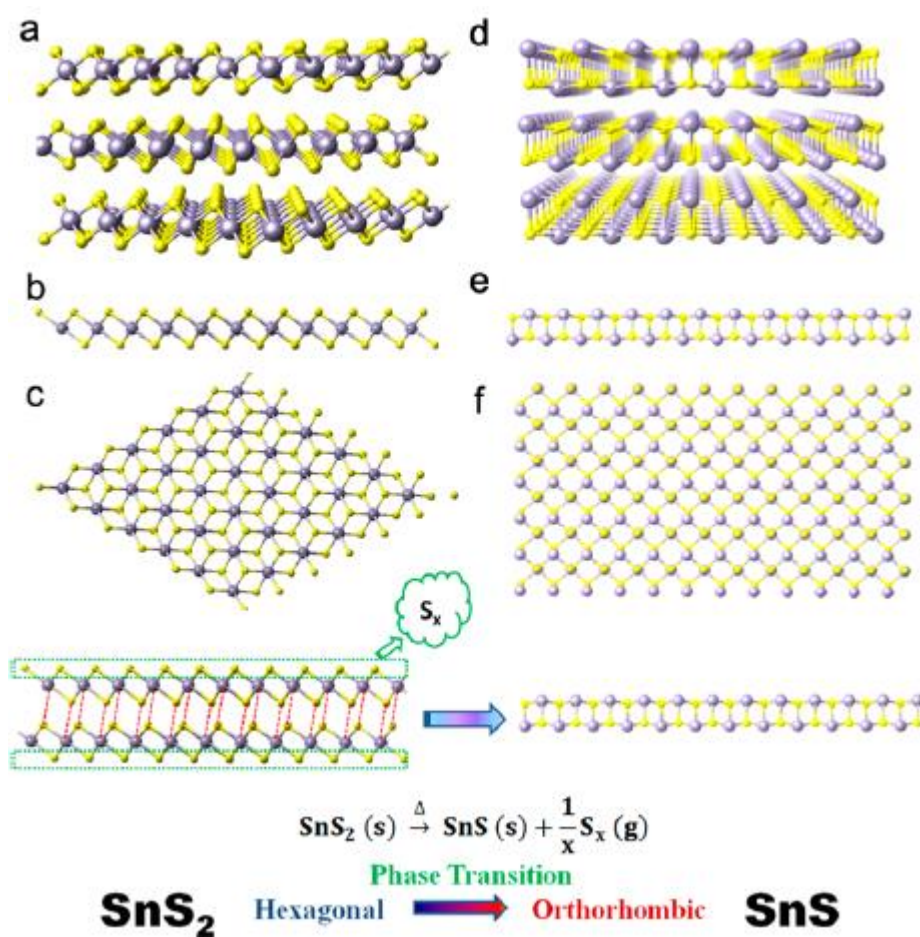


Figure 1. 12 Schematic diagram illustrating the phase transition process between SnS₂ and SnS. The crystal structures of hexagonal SnS₂ (a, b, c) and orthorhombic SnS (d, e, f) are shown in different sectional views. Adapted from Ref [49] (T. Zhou, W. Pang, C. Zhang, J. Yang, Z. Chen, H. K. Liu, and Z. Guo, ACS Nano, 8 (2014) 8323)

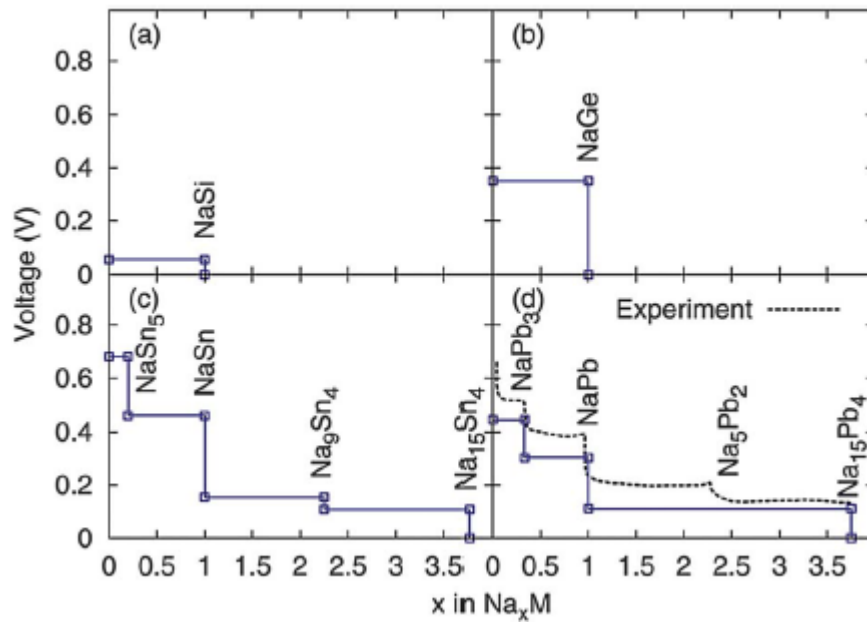


Figure 1.13 Theoretical equilibrium redox potentials of (A) Na–Si, (B) Na–Ge, (C) Na–Sn, and (D) Na–Pb. Adapted from Ref [17] (H. Pan, Y.-S. Hu, L. Chen, Energy & Environmental Science, 6 (2013) 2338-2360).

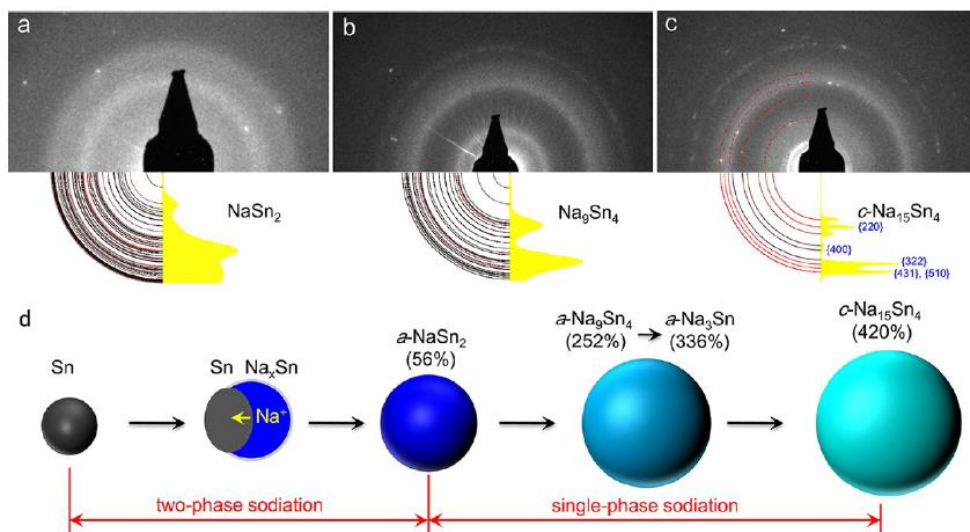


Figure 1. 14 (a-c) Three α - Na_xSn phases in the single-phase sodiation. (d) Schematic illustration of the structural evolution of Sn nanoparticles during the sodiation. Adapted from Ref [50] (J. Wang, X. Liu, S. Mao, and J. Huang, Nano Lett. 12, (2012) 5897).

1.3. Reference

- [1] M.S. Whittingham, *Chemical reviews*, 104 (2004) 4271-4302.
- [2] M.R. Palacin, *Chemical Society Reviews*, 38 (2009) 2565-2575.
- [3] G.E. Blomgren, *Journal of The Electrochemical Society*, 164 (2017) A5019-A5025.
- [4] R. Liu, J. Duay, S.B. Lee, *Chemical Communications*, 47 (2011) 1384-1404.
- [5] M. Winter, R.J. Brodd, *ACS Publications* 2004.
- [6] Y.S. Meng, M.E. Arroyo-de Dompablo, *Energy & Environmental Science*, 2 (2009) 589-609.
- [7] H. Wang, H. Dai, *Chemical Society Reviews*, 42 (2013) 3088-3113.
- [8] M.M. Thackeray, C. Wolverton, E.D. Isaacs, *Energy & Environmental Science*, 5 (2012) 7854-7863.
- [9] M. Thackeray, W. David, P. Bruce, J. Goodenough, *Materials Research Bulletin*, 18 (1983) 461-472.
- [10] L. Shi, W. Xie, Q. Ge, S. Wang, D. Chen, L. Qin, M. Fan, L. Bai, Z. Chen, H. Shen, *Int. J. Electrochem. Sci*, 10 (2015) 4696-4705.
- [11] A.K. Padhi, K.S. Nanjundaswamy, J.B. Goodenough, *Journal of the electrochemical society*, 144 (1997) 1188-1194.
- [12] S. Choi, T.-w. Kwon, A. Coskun, J.W. Choi, *Science*, 357 (2017) 279-283.
- [13] X. Zuo, J. Zhu, P. Müller-Buschbaum, Y.-J. Cheng, *Nano Energy*, 31 (2017) 113-143.
- [14] M. Armand, J.-M. Tarascon, *nature*, 451 (2008) 652.

- [15] S.H. Yu, S.H. Lee, D.J. Lee, Y.E. Sung, T. Hyeon, *Small*, 12 (2016) 2146-2172.
- [16] M.D. Slater, D. Kim, E. Lee, C.S. Johnson, *Advanced Functional Materials*, 23 (2013) 947-958.
- [17] H. Pan, Y.-S. Hu, L. Chen, *Energy & Environmental Science*, 6 (2013) 2338-2360.
- [18] V. Palomares, P. Serras, I. Villaluenga, K.B. Hueso, J. Carretero-González, T. Rojo, *Energy & Environmental Science*, 5 (2012) 5884-5901.
- [19] Z. Li, J. Ding, D. Mitlin, *Accounts of chemical research*, 48 (2015) 1657-1665.
- [20] W. Luo, F. Shen, C. Bommier, H. Zhu, X. Ji, L. Hu, *Accounts of chemical research*, 49 (2016) 231-240.
- [21] J. Peters, D. Buchholz, S. Passerini, M. Weil, *Energy & Environmental Science*, 9 (2016) 1744-1751.
- [22] H.G. Wang, W. Li, D.P. Liu, X.L. Feng, J. Wang, X.Y. Yang, X.b. Zhang, Y. Zhu, Y. Zhang, *Advanced Materials*, 29 (2017).
- [23] K. Kubota, S. Komaba, *Journal of The Electrochemical Society*, 162 (2015) A2538-A2550.
- [24] J.-Y. Hwang, S.-T. Myung, Y.-K. Sun, *Chemical Society Reviews*, 46 (2017) 3529-3614.
- [25] C. Delmas, J.-J. Braconnier, C. Fouassier, P. Hagenmuller, *Solid State Ionics*, 3 (1981) 165-169.

- [26] S.W. Kim, D.H. Seo, X. Ma, G. Ceder, K. Kang, *Advanced Energy Materials*, 2 (2012) 710-721.
- [27] H. Kim, H. Kim, Z. Ding, M.H. Lee, K. Lim, G. Yoon, K. Kang, *Advanced Energy Materials*, 6 (2016).
- [28] A.R. West, *Basic solid state chemistry*, John Wiley & Sons Inc1999.
- [29] J. Billaud, G. Singh, A.R. Armstrong, E. Gonzalo, V. Roddatis, M. Armand, T. Rojo, P.G. Bruce, *Energy & Environmental Science*, 7 (2014) 1387-1391.
- [30] N. Yabuuchi, R. Hara, M. Kajiyama, K. Kubota, T. Ishigaki, A. Hoshikawa, S. Komaba, *Advanced Energy Materials*, 4 (2014).
- [31] K. Hemalatha, M. Jayakumar, P. Bera, A. Prakash, *Journal of Materials Chemistry A*, 3 (2015) 20908-20912.
- [32] W. Kang, Z. Zhang, P.-K. Lee, T.-W. Ng, W. Li, Y. Tang, W. Zhang, C.-S. Lee, D.Y.W. Yu, *Journal of Materials Chemistry A*, 3 (2015) 22846-22852.
- [33] K.T. Lee, T. Ramesh, F. Nan, G. Botton, L.F. Nazar, *Chemistry of Materials*, 23 (2011) 3593-3600.
- [34] F. Boucher, J. Gaubicher, M. Cuisinier, D. Guyomard, P. Moreau, *Journal of the American Chemical Society*, 136 (2014) 9144-9157.
- [35] S. Yu, M. Shokouhimehr, T. Hyeon, Y. Sung, A39.
- [36] H.-W. Lee, R.Y. Wang, M. Pasta, S.W. Lee, N. Liu, Y. Cui, *Nature communications*, 5 (2014) ncomms6280.
- [37] H. Lee, Y.-I. Kim, J.-K. Park, J.W. Choi, *Chemical Communications*, 48 (2012) 8416-8418.

- [38] J. Qian, M. Zhou, Y. Cao, X. Ai, H. Yang, *Advanced Energy Materials*, 2 (2012) 410-414.
- [39] H. Hou, X. Qiu, W. Wei, Y. Zhang, X. Ji, *Advanced Energy Materials*, (2017).
- [40] M. Dahbi, N. Yabuuchi, K. Kubota, K. Tokiwa, S. Komaba, *Physical chemistry chemical physics*, 16 (2014) 15007-15028.
- [41] Y. Wen, K. He, Y. Zhu, F. Han, Y. Xu, I. Matsuda, Y. Ishii, J. Cumings, C. Wang, *Nature communications*, 5 (2014) 4033.
- [42] H. Kim, J. Hong, Y.U. Park, J. Kim, I. Hwang, K. Kang, *Advanced Functional Materials*, 25 (2015) 534-541.
- [43] L. Fu, K. Tang, K. Song, P.A. van Aken, Y. Yu, J. Maier, *Nanoscale*, 6 (2014) 1384-1389.
- [44] L. Qie, W. Chen, X. Xiong, C. Hu, F. Zou, P. Hu, Y. Huang, *Advanced Science*, 2 (2015).
- [45] P. Wang, B. Qiao, Y. Du, Y. Li, X. Zhou, Z. Dai, J. Bao, *The Journal of Physical Chemistry C*, 119 (2015) 21336-21344.
- [46] R. Alcántara, M. Jaraba, P. Lavela, J. Tirado, *Chemistry of Materials*, 14 (2002) 2847-2848.
- [47] F. Klein, B. Jache, A. Bhide, P. Adelhelm, *Physical Chemistry Chemical Physics*, 15 (2013) 15876-15887.
- [48] Z. Hu, Q. Liu, S.L. Chou, S.X. Dou, *Advanced Materials*, (2017).
- [49] T. Zhou, W. Pang, C. Zhang, J. Yang, Z. Chen, H. K. Liu, and Z. Guo, *ACS Nano*, 8 (2014) 8323-8333

- [50] J. Wang, X. Liu, S. Mao, and J. Huang, *Nano Lett.* 12, (2012) 5897–5902.
- [51] C.M. Park, H.J. Sohn, *Adv. Mater.*, 19 (2007) 2465-2468.
- [52] Y. Kim, Y. Park, A. Choi, N.S. Choi, J. Kim, J. Lee, J.H. Ryu, S.M. Oh, K.T. Lee, *Adv. Mater.*, 25 (2013) 3045-3049.
- [53] Y. Xu , Y. Zhu , Y. Liu , and C. Wang, *Adv. Energy Mater.* 2013, 3, 128–133.
- [54] J. Sun, H.-W. Lee, M. Pasta, H. Yuan, G. Zheng, Y. Sun, Y. Li and Yi Cui, *Nature Nanotechnology.*, 10 (2015) 980-985.
- [55] L. Liang, Y. Xu, C. Wang, L. Wen, Y. Fang, Y. Mi, M. Zhou, H. Zhao and Y. Lei, *Energy Environ. Sci.*, 8 (2015) 2954-2962.
- [56] J. Qian, X. Wu, Y. Cao, X. Ai, and H. Yang, *Angew. Chem. Int. Ed.*, 2013, 52, 4633-4636.

Chapter 2. Solvothermal-Derived S-doped Graphene as an Anode Material for Sodium-Ion Batteries

2.1. Introduction

Over the past few decades, electrical energy storage has received increasing attention both in the research and industry fields, because of the rapid growth in their use in portable electronic devices and energy storage systems (ESS).[1-6] Even though lithium-ion batteries (LIBs) have been regarded as the most popular power sources with many advantages such as high capacity and long cycle life, Li resources are limited and non-uniformly distributed globally. On the contrary, sodium is abundant, inexpensive and ubiquitous.[7] Thus, sodium-ion batteries (SIBs) have recently attracted a great deal of attention as promising alternatives to LIBs. However, graphite, which is a commercially available anode material for LIBs, is not suitable for application in SIBs owing to the larger size of sodium ions precluding for intercalation into the interlayers of graphite.[8]

Various carbonaceous materials have been applied as potential anode materials for SIBs, including hard carbon, amorphous carbon, carbon black, activated carbon, carbon fibers, and graphene.[9-11] Furthermore, different morphologies of these carbon-based materials such as porous carbon, hollow carbon spheres and porous carbon nanofibers have shown different electrochemical properties.[12-14] These results indicate that the battery properties, especially in terms of capacity and cycle stability, could be effectively

adjusted by the judicious control of physical properties, such as pore size and interlayer distance. In addition, heteroatom doping (e.g., S, P and N) is also an efficient means to tune the chemical and physical properties of carbonaceous materials,[15-23] as it can modulate electronic properties by producing defects and porosities, as well as increase the interlayer distance of carbon. Li et al. synthesized S-doped disordered carbon that exhibited a high reversible capacity of 516 mAh g⁻¹ at 20 mA g⁻¹. [8] Yang et al. prepared S-doped N-rich carbon nanosheets, which achieved a reversible capacity of 350 mAh g⁻¹ at 50 mA g⁻¹, which is much higher than N-doped carbon.[24] In addition, Qie et al. demonstrated that S-doping could enlarge the interlayer distances of carbon materials. Moreover, they also claimed that S-doped carbon was more suitable than N-doped carbon for SIBs anodes, because doped sulfur can act as a redox site for reaction with sodium ions and enlarge interlayer distance.[25, 26]

Recently, a gram-scale synthetic method was developed to produce solvothermal carbon nanomaterials using liquid precursors. These carbon materials had sheet-like two dimensional (2D) nanostructures.[15, 27] Choucair et al. first synthesized solvothermal carbon using ethanol as a source, and demonstrated that solvothermal carbon can be categorized within the graphene family.[27] Solvothermal graphene showed a higher degree of disorder than traditional graphene. Our group successfully converted S-containing organic molecules (dimethyl sulfoxide, DMSO) into S-doped solvothermal graphene via a modified thermal process. Compared with traditional doping processes (e.g., chemical vapor deposition; segregation growth and post treatment, etc.), the

conditions employed for this thermal process were relatively mild.[28-30] In this study, the sodium storage properties of S-doped solvothermal graphene (S-SG) and pristine solvothermal graphene (SG) have been investigated. S-SG exhibited a high reversible capacity of 380 mAh g⁻¹ after 300 cycles at 100 mA g⁻¹, excellent rate performance of 217 mAh g⁻¹ at 3200 mA g⁻¹. In addition, it showed excellent cycling performance at 2.0 A g⁻¹ during 1000 cycles with no capacity fade.

2.2. Experimental section

2.2.1. Reagents

DMSO (99.7%) was purchased from Acros Organics (NJ, USA). Hydrochloric acid (35-37%), sodium metal, sodium hydroxide (NaOH, 98%), and methanol (99%) were purchased from Samchun Pure Chemical (Seoul, South Korea). Deionized water was filtered using a water purification system. Unless otherwise stated, all chemicals were used as-received without further purification.

2.2.2. Synthesis method of S-SG

S-SG was synthesized according to a previously reported method^[6a]. Briefly, a mixture of DMSO (20 mL) and NaOH (4 g) was added into a flask and heated at 300 °C under a flow of nitrogen gas. Under these reflux conditions, the colorless liquid turned dark and resulting in black cake-like substances. These black samples were washed with deionized water several times, and dried in a

vacuum oven at 70 °C.

2.2.3. Synthesis method of pristine SG

Pristine SG was also synthesized according to a previously reported literature method.^[6a] 15 g of sodium metal and 50 mL of methanol were charged to a Teflon-lined autoclave, which was then sealed and heated at 190 °C for 36 h. After the autoclave was cooled down to room temperature, the resulting solid was annealed at 500 °C under a flow of nitrogen gas. The product was washed with a 10wt% aqueous HCl solution and deionized water several times. Caution: The sodium metal-containing solid sample can easily catch fire, when exposed to air.

2.2.4. Materials characterization

Field-emission SEM (FE-SEM, SUPRA 55VP) and TEM (JEM-2100F) coupled with EDS (Oxford Instrument) were employed to examine the morphology and composition of the S-SG and pristine SG samples. The crystal structures were determined by XRD (Bruker D-5005) using Cu K α radiation at $\lambda = 1.54\text{\AA}$. The Raman spectra were obtained using a Dongwoo DM500i Raman spectrometer. XPS was carried out on a Sigma Probe instrument (ThermoFisher Scientific) with Al K α (1486.8 eV) as the X-ray source. Elemental analysis was carried out with a Thermo Scientific Flash 2000 organic elemental analyzer installed at the National Center for Inter-university Research Facilities (NCIRF) at Seoul National University. Nitrogen adsorption and desorption isotherms were

obtained using a Micromeritics ASAP 2020 surface area and porosity analyzer.

2.2.5 Electrochemical characterization of materials

Electrodes were made by mixing the 70 wt% of active material, 15 wt% of super P and 15 wt% of poly (acrylic acid) in *n*-methyl-2-pyrrolidinone. Afterwards, the slurries were dried in a vacuum oven overnight. Sodium metal was used as the counter electrode, while a glass fiber GF/C (Whatman) and 1.0 M NaClO₄ in ethylene carbonate (EC)/propylene carbonate (PC) (1:1 by volume) were used as the separator and the electrolyte, respectively. In addition, 5wt% fluoroethylene carbonate (FEC) was added to the electrolyte as an additive. The loading levels of the active materials were 1 mg cm⁻². 2032-type coin cells were assembled in an Ar-filled glove box and tested using a WBCS3000 cycler (WanATech) in the range from 0.01 V to 3.0 V (vs. Na⁺/Na) at 25 °C.

2.3. Results and discussion

2.3.1 Synthesis and characterization of S-SG and SG

For preparation of the desired S-SG powders, the carbon- and sulfur-containing precursor (i.e., DMSO) was heated at reflux under inert conditions until formation of the desired black product was observed (Figure 2.1). Similarly, the pristine SG was synthesized via a modified thermal process using methanol as the carbon source. As shown in the scanning electron microscopy (SEM) image presented in Figure 2.2 a, the as-prepared S-SG samples are porous, and composed of nanosheets. In addition, the transmission electron microscopy

(TEM) image showed that the S-SG sample presents a thin and crumpled morphology (Figure 2.3a.), while the high resolution TEM image (Figure 2.3b) clearly shows that the interlayer distance is significantly larger (~ 0.41 nm) than that of graphite (~ 0.34 nm). This expanded interlayer spacing is expected to facilitate the insertion of large Na ions between the layers. The SEM and TEM images of pristine SG was shown in Figure 2.2b and Figure 2.4.

Figure 2.5 presents the TEM image and corresponding energy-dispersive X-ray spectroscopy (EDS) mapping images of S-SG, which show that elemental sulfur was homogeneously distributed in the S-SG samples. Based on the elemental analysis results (Table 2.1), the sulfur content of the S-SG was 21.8 wt%.

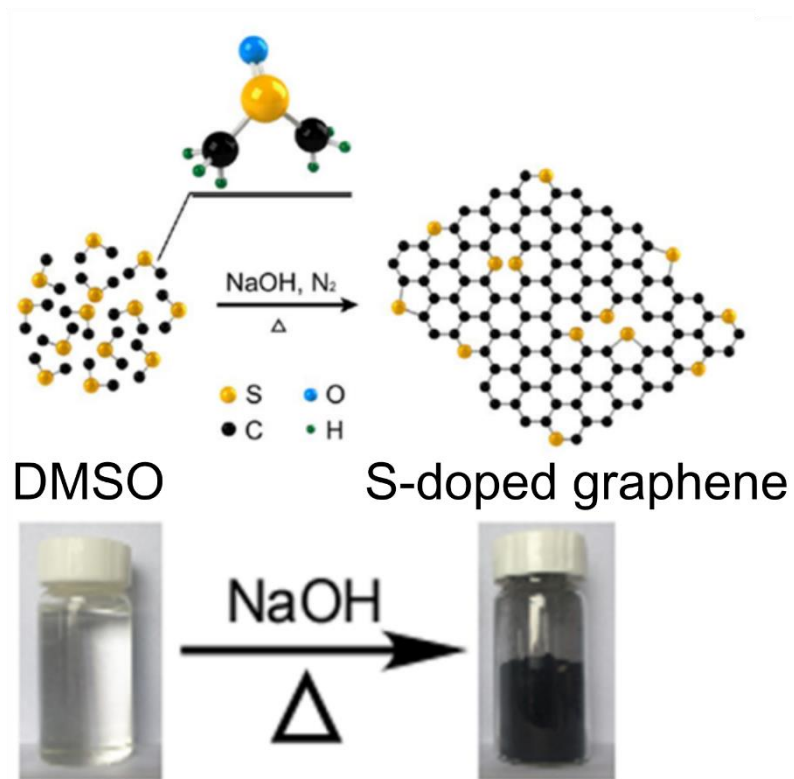


Figure 2. 1 Scheme of synthesis illustration of S-SG and A photographic image of DMSO and S-SG.

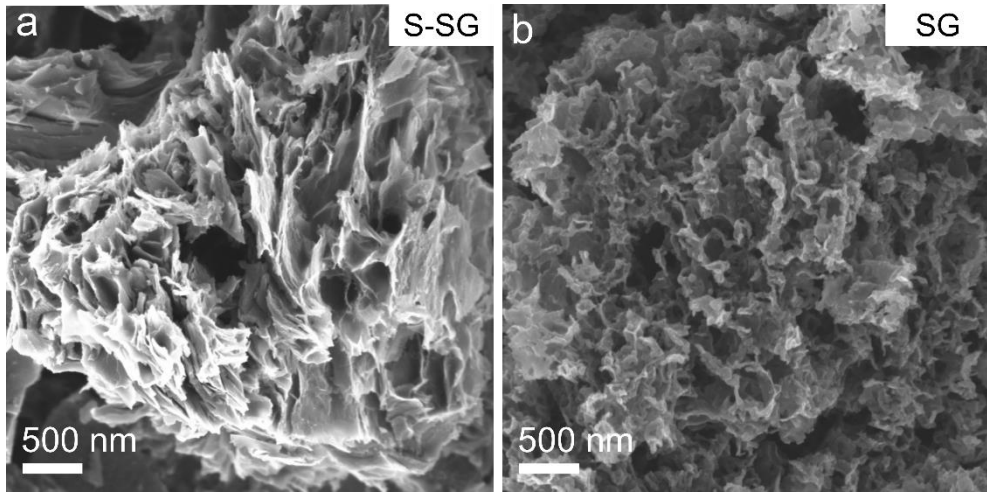


Figure 2. 2 SEM images of S-SG and SG.

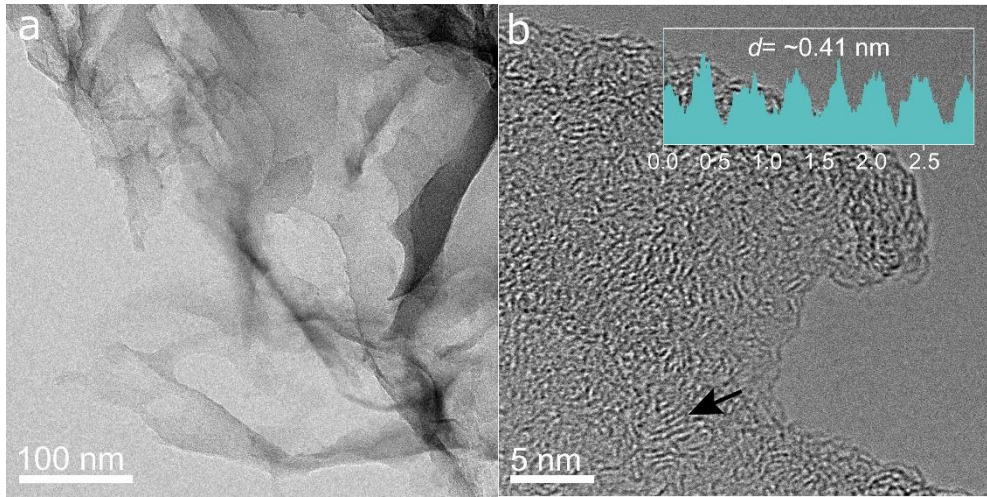


Figure 2. 3 (a) TEM and (b) high-resolution TEM images of S-SG.

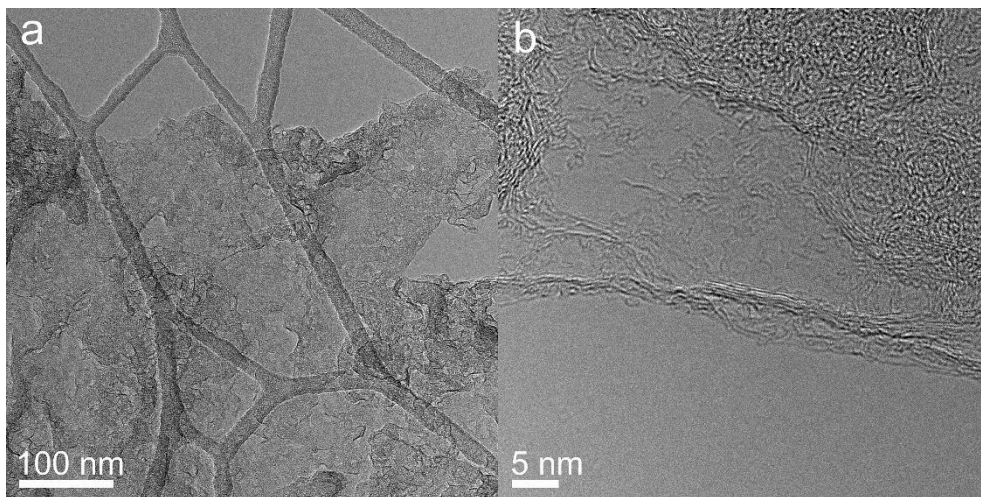


Figure 2. 4 (a) TEM and (b) high-resolution TEM images of pristine SG.

Table 2. 1 Elemental analysis data for S-SG and pristine SG.

Sample	% Composition/Mass				
	C	H	N	S	O
S-doped solvothetmal graphene	71.77	1.24	0.06	21.80	4.93
Pristine solvothetmal graphene	88.83	1.50	-	-	9.48

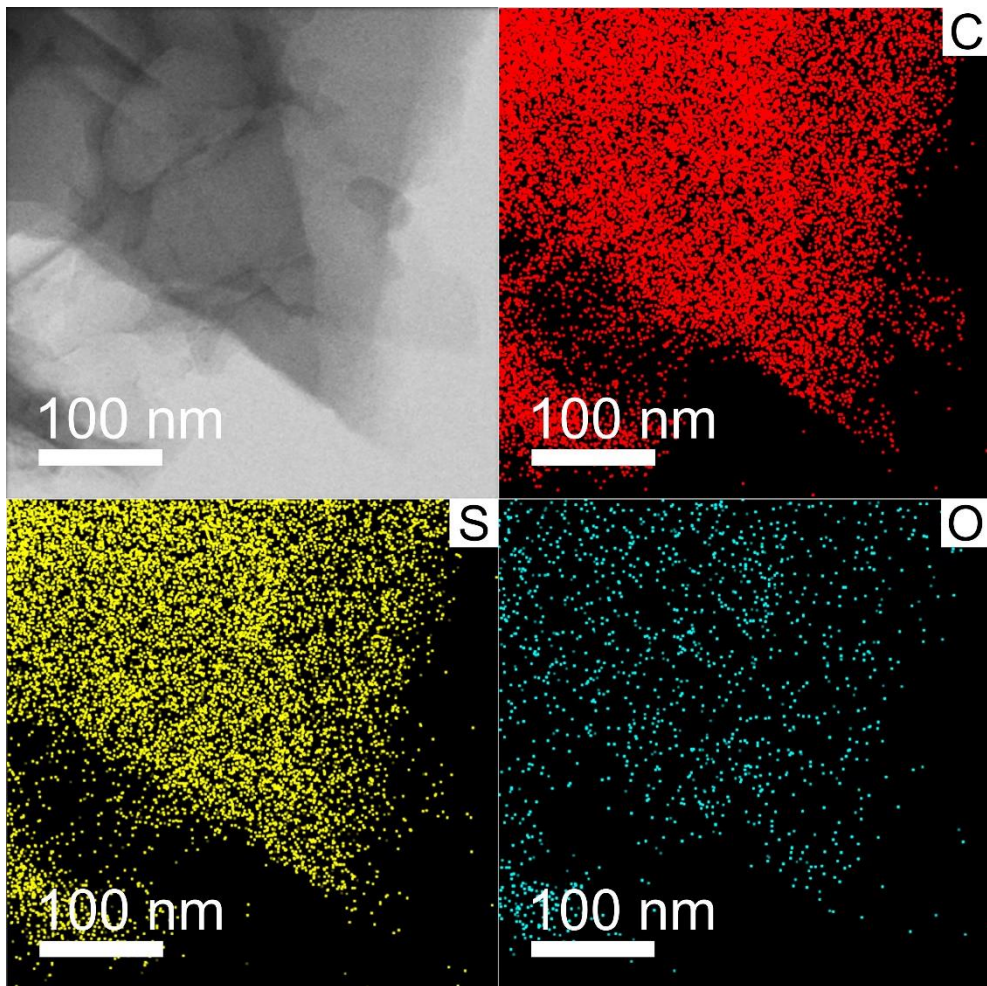


Figure 2. 5 TEM image and EDS elemental mapping of S-SG.

To better understand the chemical states of the S-SG and pristine SG, X-ray photoelectron spectroscopy (XPS) was carried out. In the XPS survey spectra (Figure 2.6a), the sulfur peaks could be clearly detected in the S-SG sample, while only carbon and oxygen were present in the pristine SG sample. It is worth noting that the peak ratio of oxygen to carbon is much lower in the S-SG sample. Also, much smaller peaks from C-O (286.5 eV) and C=O bonds (288.2 eV) were observed, compared to peaks from C-C bonds (284.5 eV) in the high resolution C1s XPS spectrum of S-SG (see Figure 2.6c).[15] The high resolution S2p XPS spectrum of S-SG exhibited three peaks at binding energies of 163.6, 164.8, and 168.5 eV, which correspond to S2p_{3/2}, S2p_{1/2}, and the oxidized sulfur groups, respectively (Figure 2.6b).[15, 25] These observations suggest that the S and C atoms are covalently bonded. Furthermore, the Raman spectra of both S-SG and pristine SG showed broad and merged disorder-induced D-bands and graphite G-bands at around 1,350 and 1,600 cm⁻¹ (Figure 2.7). In the X-ray diffraction (XRD) results (Figure 2.8), broad peaks located at 22.3° and 44.3° were observed for both S-SG and the pristine SG, corresponding to the (002) diffraction of the graphitic layered structure and the (100) diffraction of graphite, respectively.[8, 27, 31]

Broad and diffuse ring patterns are observed in selected area electron diffraction (SAED) patterns of S-SG and pristine SG (Figure 2.9), confirming that a stacking number of carbon layers in S-SG and pristine SG is smaller than that of graphite. This is in good agreement with XRD and Raman results. [20] The interlayer distances were calculated based on Bragg's law, and were found to be about 0.40

nm for both samples, thereby confirming the TEM result presented in Figure 2.1d. Moreover, the nitrogen adsorption and desorption isotherms and pore size distributions of the S-SG and pristine SG were also investigated (Figure 2.10). The adsorption isotherms are classified into several types, and the types of isotherms of S-SG and pristine SG could be classified as type IV isotherms, indicating the presence of mesoporous structures with Brunauer-Emmett-Teller (BET) surface areas of 308 and 741 m² g⁻¹, respectively.[15] The Barret-Joyner-Halenda (BJH) adsorption average pore diameters of S-SG and SG were determined to 10.4 and 9.4 nm, respectively (Figure 2.10b).

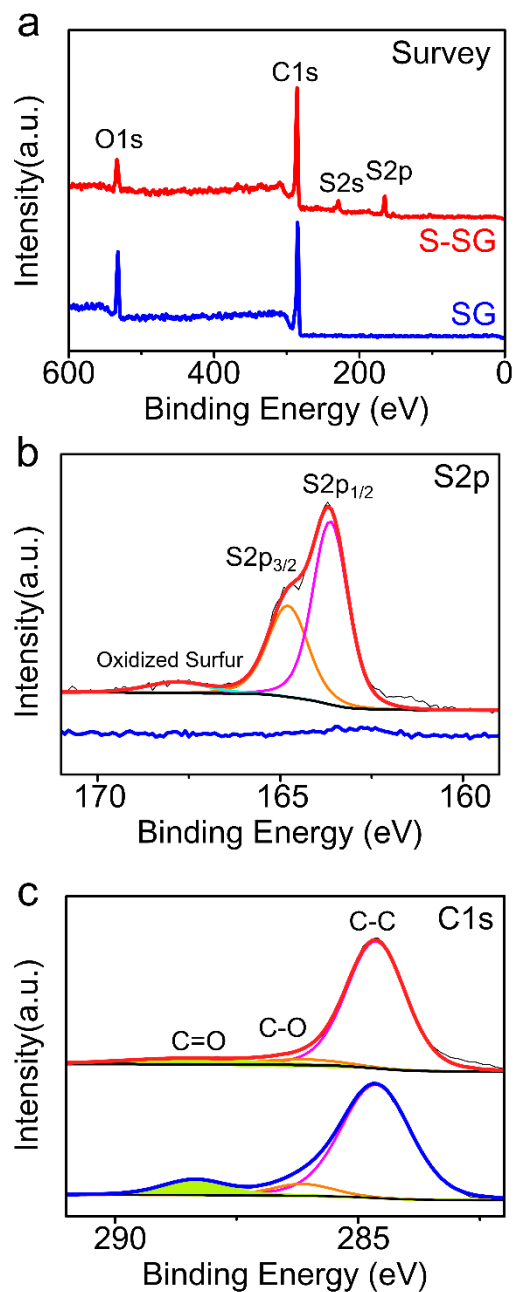


Figure 2. 6 S-SG and pristine SG XPS spectra of (a)XPS survey spectra, (b) high resolution S2p with S2p_{3/2}, S2p_{1/2}, and oxidized sulfur, and (c) high resolution C1s spectra.

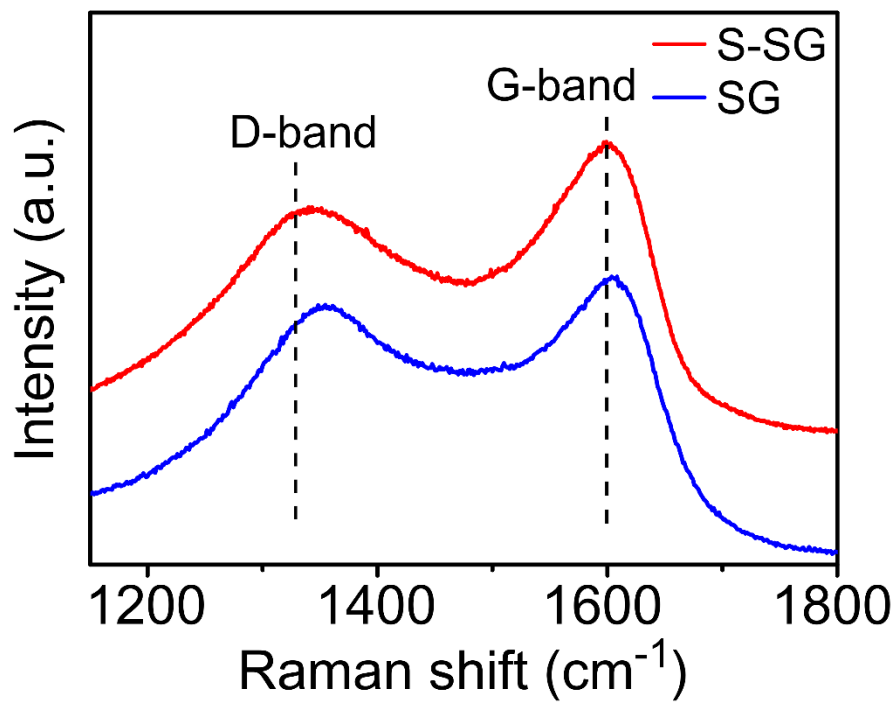


Figure 2. 7 Raman spectrum of S-SG and pristine SG.

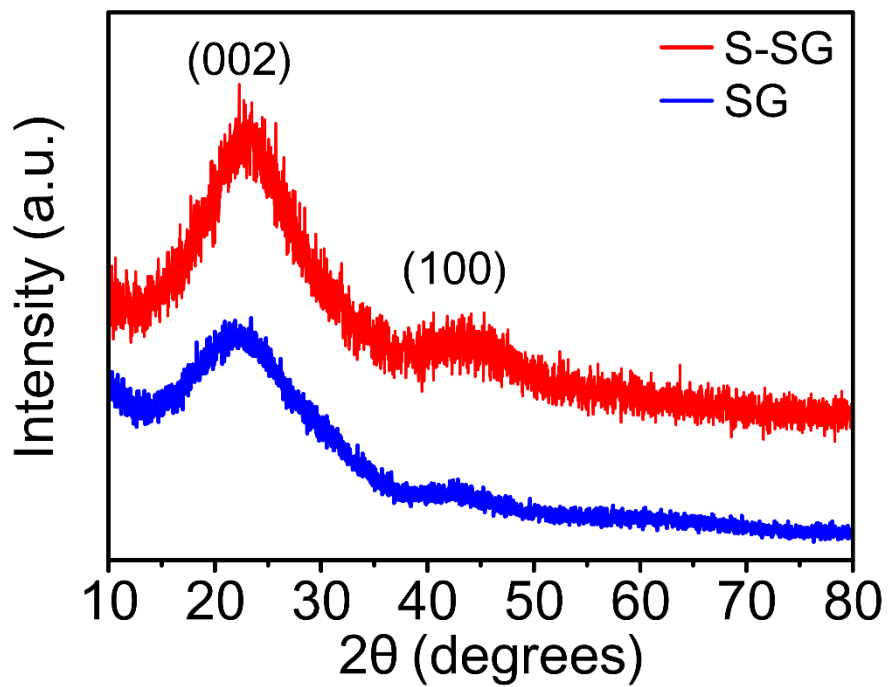


Figure 2. 8 XRD patterns of S-SG and pristine SG.

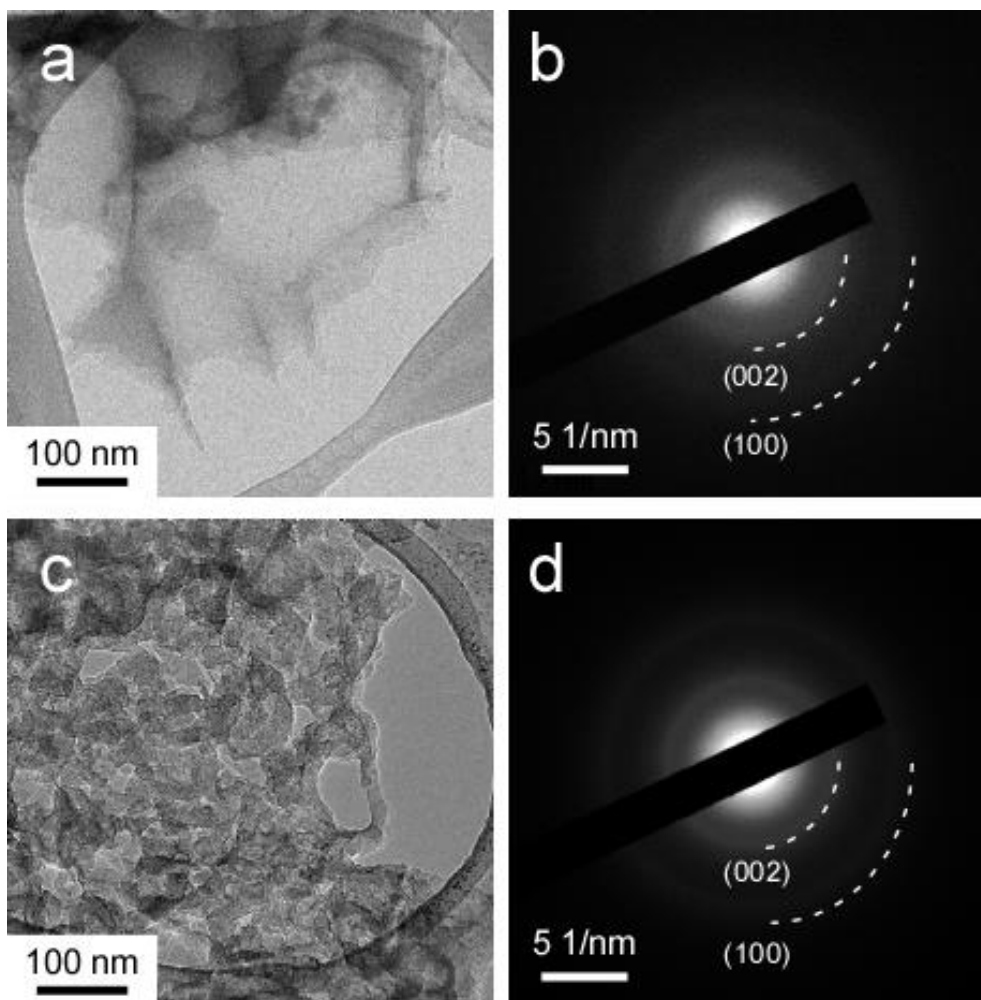


Figure 2. 9 The TEM images (a) S-SG and (c) pristine SG, and (b, d) corresponding SAED patterns, respectively.

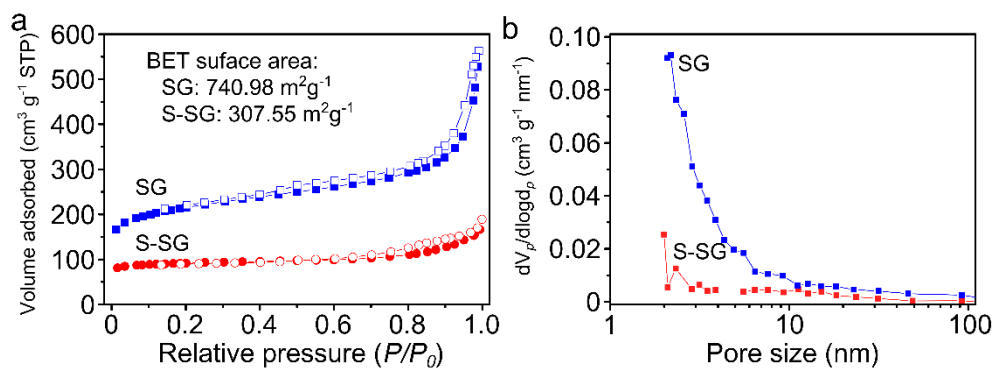


Figure 2. 10 (a) Nitrogen-adsorption/desorption isotherms of S-SG and pristine SG. (b) BJH pore size distributions of S-SG and pristine SG as calculated from the adsorption isotherms.

2.3.2 Electrochemical performance of S-SG and SG

To evaluate the electrochemical properties of S-SG and the pristine SG, coin cells were galvanostatically discharged/charged in the range of 0.01-3.0 V (vs. Na⁺/Na). Figure 2.11a and 2.11b present the voltage profiles of S-SG and pristine SG electrodes during the initial 5 cycles at a current density of 100 mA g⁻¹. As indicated in Figure 2.11b, pristine SG delivered initial discharge and charge capacities of 1045.4 and 302.4 mAh g⁻¹, respectively. The initial Coulombic efficiency of pristine SG was 28.9%. On the contrary, S-SG exhibited a significantly improved Coulombic efficiency of 55.6%. The Coulombic efficiency of the S-SG is almost twice than that of pristine SG because S-SG has lower surface area (Figure 2.7a) and lower oxygen content (Table 2.1). Also, S-SG delivered higher sodiation/desodiation capacities of 877.8/488.0 mAh g⁻¹ (Figure 2.11a). The high reversible capacity of over 400 mAh g⁻¹ was retained during subsequent cycles for the S-SG electrode.

The initial three cyclic voltammograms (CVs), which were obtained at a scan rate of 0.1 mV s⁻¹, are shown in Figure 2.11c and 2.11d for S-SG and pristine SG, respectively. In the case of the pristine SG, two well-defined peaks at about 1.0 V and 0.4 V disappeared after first reduction. The peak observed at 1.0 V was attributed to the irreversible reaction of the functional groups with sodium ions. Another cathodic peak at 0.4 V is related to formation of solid electrolyte interphase (SEI) layer.[32-35] Contrary to CVs of the pristine SG, two additional redox couples were observed at 1.6/2.2 and 1.1/1.8 V in CVs of S-SG. These

redox couples are resulted from the reaction of doped sulfur with Na ions, so these are often found in CVs of room temperature Na-S batteries [8, 36]. Reduction peak at 1.6 V is ascribed to reaction between S and Na ions to form Na_2S_2 . The second cathodic peak at 1.1 V is related to reduction of Na_2S_2 to Na_2S . It is worthwhile to note that S-SG presents a number of advantages as an SIB anode material compared to pristine SG or other graphene with oxygen-functional groups. The electrochemically active sulfur can enhance the capacity, while the reaction between S and Na is significantly more reversible than that between O and Na, in addition to exhibiting lower voltage hysteresis. Furthermore, S-SG has a particularly high lattice spacing related to that of pristine SG, which can facilitate the insertion of Na ions into the layers, even in the presence of lower quantities of oxygen (see Table 2.1 for elemental analysis, also discussed in XPS section above).

The cycle performances of pristine SG and S-SG at current densities of 100 and 200 mA g^{-1} are displayed in Figure 2.12. The S-SG delivered a reversible capacity of 379.5 mAh g^{-1} at 100 mA g^{-1} in the 300th cycle with a negligible capacity fade during 300 cycles, while the capacity of pristine SG kept decreasing to 182.8 mAh g^{-1} at the 300th cycle. The reversible capacity of S-SG is almost twice as high as that of pristine SG, and its Coulombic efficiency is over 99.8% at 100 mA g^{-1} . Interestingly,

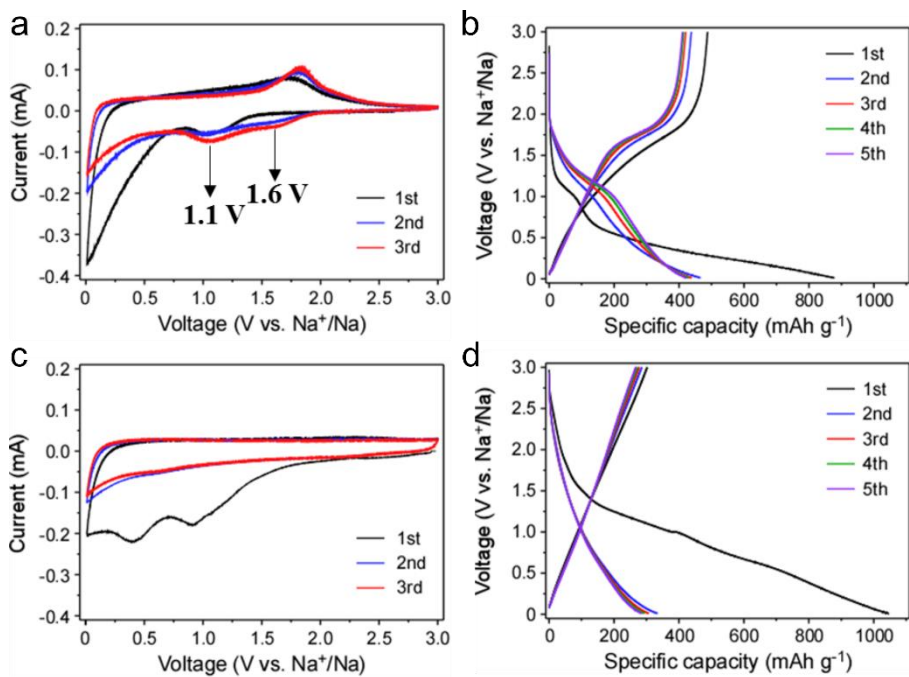


Figure 2. 11 Voltage profiles of (a) S-SG and (b) pristine SG at a current density of 100 mA g⁻¹. Cyclic voltammograms of (c) S-SG and (d) pristine SG at a scan rate of 0.1 mV s⁻¹.

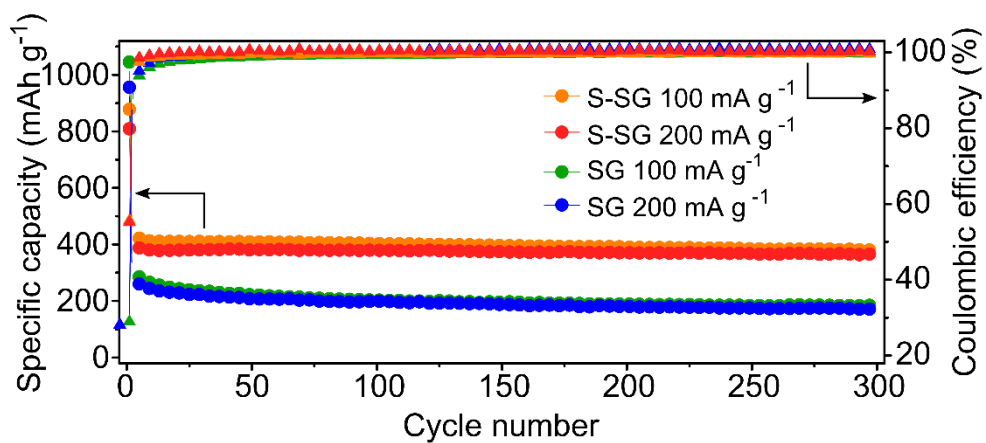


Figure 2. 12 Cycle performance of pristine SG and S-SG at current densities of 100 and 200 mA g⁻¹.

the capacity and cycle performance of both S-SG and pristine SG at 200 mA g⁻¹ are similar at 100 mA g⁻¹, suggesting that the rate-capabilities of both materials are excellent. The clear capacity fade during the initial 50 cycles in pristine SG, which is likely to be due to the less reversible reaction between O and Na, is rarely observed in S-SG. Even at higher current density of 500 mA g⁻¹, its discharge capacity is over 300 mAh g⁻¹ (Figure 2.13).

As shown in Figure 2.14, the rate properties of the pristine SG and S-SG were evaluated by varying the current density stepwise from 50 to 3200 mA g⁻¹, and then back to 50 mA g⁻¹. Both S-SG and pristine SG showed high cycle stability at all current densities, including the very high current density of 3200 mA g⁻¹. However, S-SG showed much higher capacities than those of pristine SG, which were 436.0, 398.1, 365.5, 329.0, 290.3, 251.2, 217.1, and 422.6 mAh g⁻¹ at 50, 100, 200, 400, 800, 1600, 3200, and 50 mA g⁻¹, respectively. In particular, the capacity of S-SG remained at over 200 mAh g⁻¹ even at 3200 mA g⁻¹, while the capacity of pristine SG dropped to 147.8 mAh g⁻¹. The capacities of S-SG recovered to high values when the current density decreased back to 50 from 3200 mA g⁻¹, indicating that the structure of S-SG is well-maintained even after high rate cycling. The high rate capability of S-SG is resulted from S-doping, which increases electrical conductivity and facilitate the Na ion transport by expanding interlayer spacing. To further explain the slight capacity difference at same current density during the constant current cycling test (Figure 2.12), and stepwise current cycling test (Figure 2.14), the voltage profiles and corresponding differential capacities were plotted in Figure 2.15. As can be seen

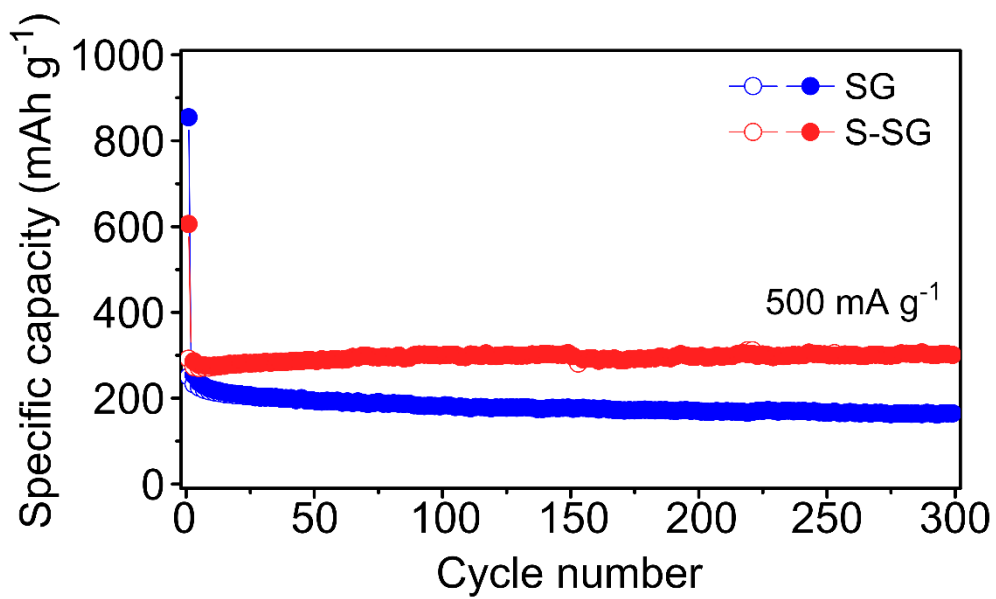


Figure 2. 13 Cycle performance of S-SG and pristine SG at a current density of 500 mA g⁻¹.

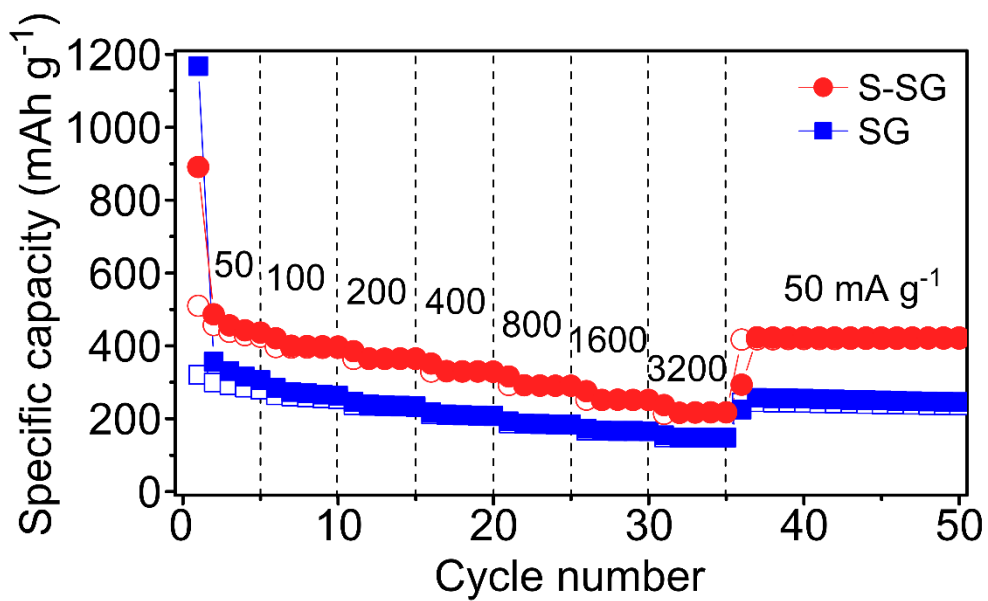


Figure 2. 14 Rate performance of pristine SG and S-SG at different current densities.

in Figure 2.15, the reaction voltage shifted during the initial cycles, which is attributed to activation process of the reaction between doped sulfur and Na ions. During this process, the total capacity also slightly changes, and this change is more dramatic in the lower current density (Figure 2.15a, 2.15b, and 2.16). Therefore, the capacities at same rate in different cycling sequences (constant current cycling test, and stepwise current cycling test) can be slightly different due to the different degree of activation occurs in two different cycling).

The cycle performance of S-SG at 2.0 A g^{-1} is shown in Figure 2.17. As indicated, after the initial cycle, the specific capacity increased continuously during the initial cycles, especially at high current densities, as is often observed for carbonaceous materials.[8, 26, 37] Once the capacity is stabilized after about 100 cycles ($> 250 \text{ mAh g}^{-1}$), it was maintained for 900 cycles without capacity fade. The electrochemical properties of S-SG and the pristine SG were compared with those of other reported materials in Table 2.2, including the carbon materials and metal oxides.[38-40] Notably, S-SG exhibited the highest electrochemical performance among them. In addition, pristine SG also exhibited relatively high cycle stability for significant periods, when compared to other un-doped carbon materials, showing that solvothermal method is a superior way to prepare graphene for SIB anodes.

The main reasons for the excellent cycle performance of solvothermal graphene are likely due to the large interlayer distances, highly disordered structures and greater number of active sites for Na ion storage than others. In addition, by doping with sulfur, as well as lowering the oxygen content, the capacity and cycle

performance of S-SG were significantly enhanced.

Electrochemical impedance spectroscopy (EIS) was performed before and after the 1st cycle for pristine SG and S-SG. As shown in Figure 2.18a, each cells exhibit only one semicircle at high frequencies before cycling. The semicircle of S-SG is much smaller than that of pristine SG before cycling, indicating that the charge transfer resistance of S-SG (R_{ct} : 282.3 Ω) decreased with surface area decrease by high doping level of sulfur. After the 1st cycle, two semicircles were showed in high and medium frequencies indicating that the formation of the SEI film. As can be seen in Figure 2.18b, both samples' semicircles are decreased. From the fitted results, obtained according to the equivalent circuit shown in inset of Figure 2.18b, both the charge transfer resistance and the SEI film resistance of S-SG (R_{ct} :154.9 Ω , R_{SEI} : 14.2 Ω) were much lower than those of the pristine SG (R_{ct} : 281.1 Ω , R_{SEI} : 93.8 Ω). Demonstrating that S-doping in solvothermal graphene decreases both the SEI layer resistance (R_{SEI}) and charge transfer resistance (R_{ct}).

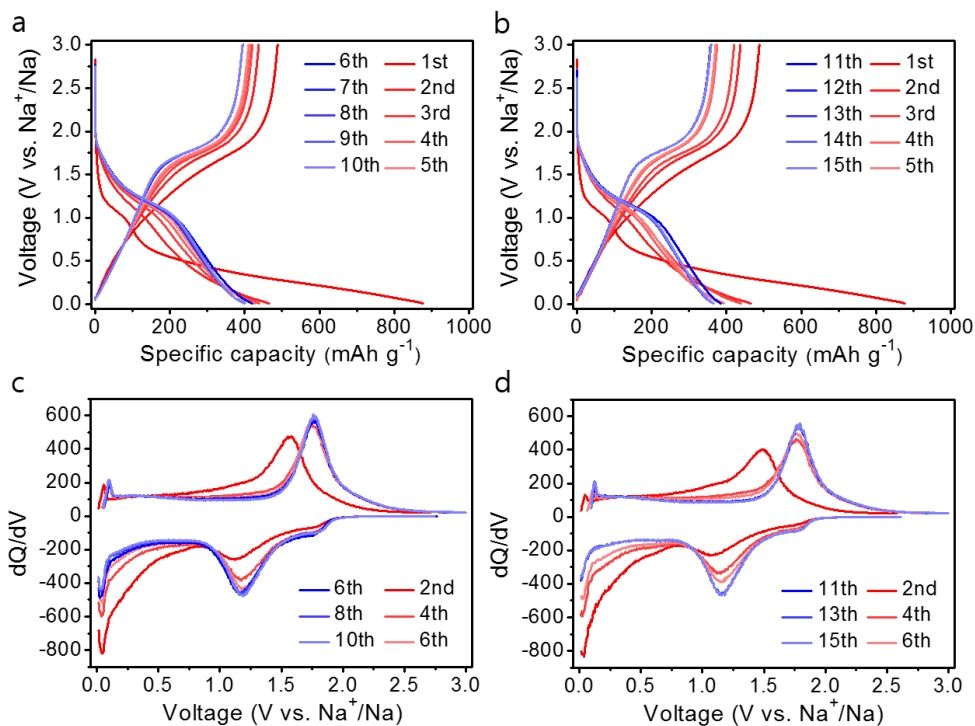


Figure 2. 15 The voltage profiles of S-SG at a current density of (a) 100 mAh g⁻¹ (red: from constant current cycling, blue: from stepwise current cycling) and (b) 200 mAh g⁻¹ (red: from constant current cycling, blue: from stepwise current cycling); the differential capacity plots of S-SG at a current density of (c) 100 mAh g⁻¹ (red: from constant current cycling, blue: from stepwise current cycling) and (d) 200 mAh g⁻¹ (red: from constant current cycling, blue: from stepwise current cycling).

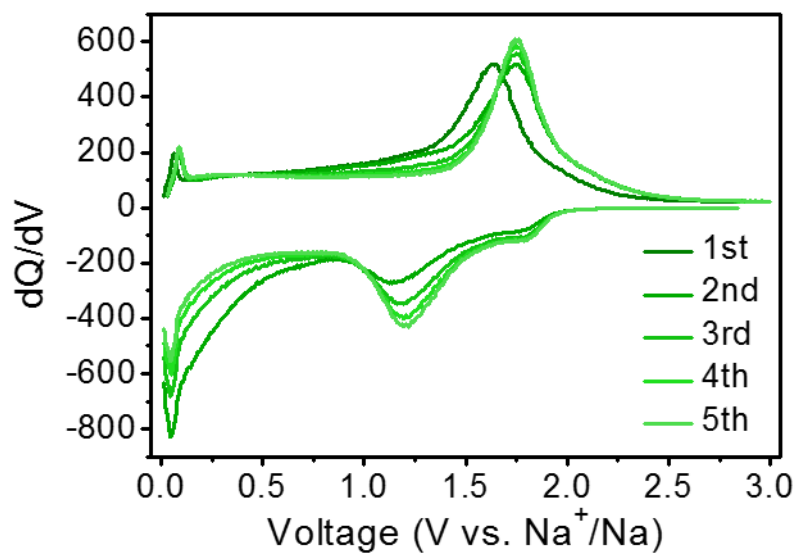


Figure 2. 16 The differential capacity plots of S-SG at a current density of 50 mAh g^{-1} .

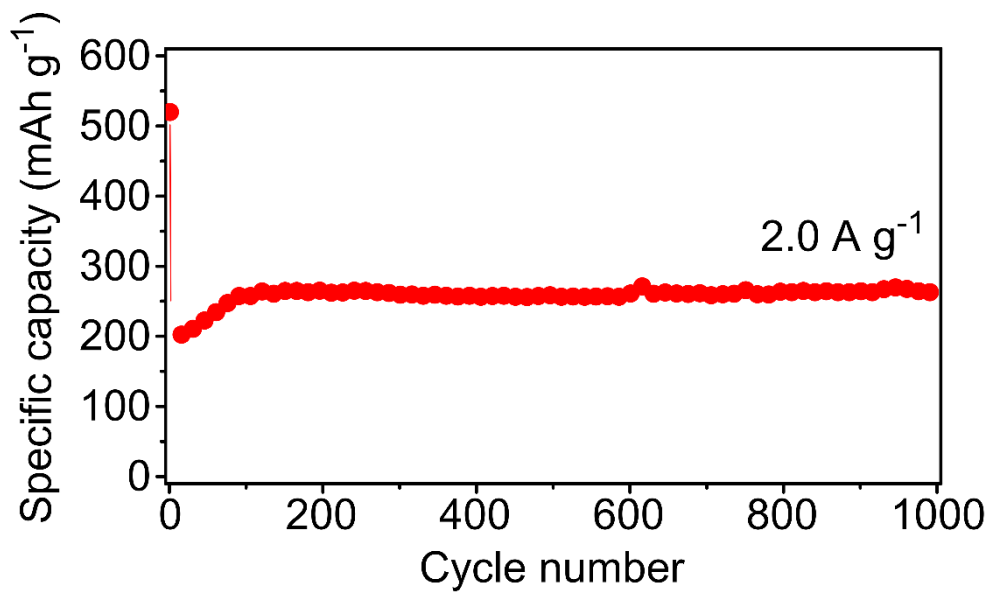


Figure 2. 17 Cycle performance of S-SG at a current density of 2.0 A g⁻¹.

Table 2. 2 Electrochemical performances of various carbon-based materials as sodium-ion battery anode materials.

Samples	Current density mA g ⁻¹	Initial discharge capacity mAh g ⁻¹	Reversible capacity mAh g ⁻¹ (at the cycle no.)	Ref.
S-doped disordered carbon	20	887	271 (1000th cycle)	[8]
N/O-doped carbon nanobubbles	100	~520	120 (30th cycle)	[17]
N-doped carbon nanotube	50	378.3	175.5 (300th cycle)	[18]
N-doped porous carbon sphere	200	635.8	206 (600th cycle)	[19]
N-doped 3D graphene foams	500	852.6	594 (80th cycle)	[20]
N/P-doped carbon microspheres	100	742	~200 (90th cycle)	[21]
S/N-doped carbon nanosheets	50	954	350 (100th cycle)	[24]
S-doped carbon	500	640	303.2 (700th cycle)	[25]
S-doped flexible graphene films	100	676	244 (300th cycle)	[26]
Reduced graphene oxide (RGO)	40	~780	174.3 (250th cycle)	[31]
Co ₃ O ₄ /CNTs	50	~550	403 (100th cycle)	[38]
MoS ₂ /graphene	20	~1700	~400 (100th cycle)	[39]
SnO ₂ /graphene	20	1942.0	~700 (100th cycle)	[40]
SG	100	1045.4	182.8 (300th cycle)	This work
S-SG	100	877.7	380.0 (300th cycle)	This work

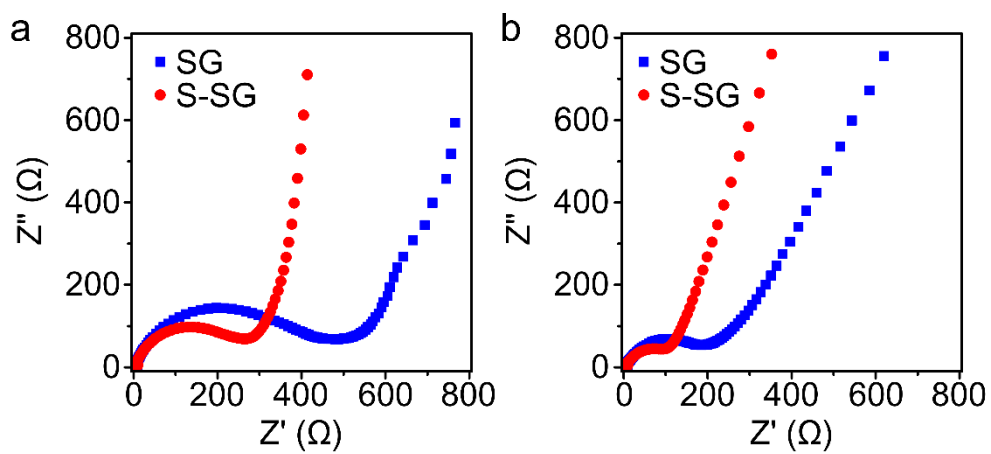


Figure 2. 18 Electrochemical impedance spectrum for S-SG and pristine SG (a) before cycling, and (b) after 1 cycle.

2.4. Conclusions

In Summary, solvothermal-derived sulfur-doped graphene (S-SG) was synthesized via a simple, economical, one-pot method as an anode electrode material for sodium-ion batteries (SIBs). We found that the prepared S-SG exhibited a highly disordered structure, a large interlayer distance, and large numbers of active sites. As an anode for SIB, S-SG exhibited a high reversible capacity of 380 mAh g^{-1} after 300 cycles at 100 mA g^{-1} , an excellent rate performance of 217 mAh g^{-1} at a particularly high current density of 3200 mA g^{-1} , and a superior cycling performance of 263 mAh g^{-1} at 2.0 A g^{-1} over 1000 cycles. To the best of our knowledge, S-SG exhibited the best electrochemical performance of other previously reported S-doped carbon materials. For comparison, pristine SG was also prepared and exhibited a high performance of 182.8 mAh g^{-1} at 100 mA g^{-1} after 300 cycles. It could be concluded that solvothermal-derived carbon materials with high levels of sulfur doping and a highly disordered structure are suitable for use as anode materials for high-performance SIBs. Indeed, we expect that such solvothermal-based carbon materials can be further extended to other energy-related applications.

2.5. References

- [1] J. Sun, H.W. Lee, M. Pasta, H. Yuan, G. Zheng, Y. Sun, Y. Li, Y. Cui, *Nat. Nanotechnol.* 10 (2015) 980-985.
- [2] N. Yabuuchi, K. Kubota, M. Dahbi, S. Komaba, *Chem. Rev.* 114 (2014) 11636-11682.
- [3] S. Wu, R. Ge, M. Lu, R. Xu, Z. Zhang, *Nano Energy* 15 (2015) 379-405.
- [4] S.-H. Yu, B. Quan, A. Jin, K.-S. Lee, S.H. Kang, K. Kang, Y. Piao, Y.-E. Sung, *ACS Appl. Mater. Interfaces* 7 (2015) 25725-25732.
- [5] L. Ni, Z. Wu, G. Zhao, C. Sun, C. Zhou, X. Gong, G. Diao, *Small* 13 (2017) 1603466.
- [6] X. Lu, C. Wang, F. Favier, N. Pinna, *Adv. Energy Mater.* 7 (2017) 1601301.
- [7] Y. Li, Y. Lu, C. Zhao, Y.-S. Hu, M.-M. Titirici, H. Li, X. Huang, L. Chen, *Energy Storage Mater.* 7 (2017) 130-151.
- [8] W. Li, M. Zhou, H. Li, K. Wang, S. Cheng, K. Jiang, *Energy Environ. Sci.* 8 (2015) 2916-2921.
- [9] Z. Li, Z. Jian, X. Wang, I.A. Rodriguez-Perez, C. Bommier, X. Ji, *Chem. Commun.* 53 (2017) 2610-2613.
- [10] X.-F. Luo, C.-H. Yang, Y.-Y. Peng, N.-W. Pu, M.-D. Ger, C.-T. Hsieh, J.-K. Chang, *J. Mater. Chem. A* 3 (2015) 10320-10326.
- [11] F. Legrain, J. Sottmann, K. Kotsis, S. Gorantla, S. Sartori, S. Manzhos, *J. Phys. Chem. C* 119 (2015) 13496-13501.
- [12] J. Ye, J. Zang, Z. Tian, M. Zheng, Q. Dong, *J. Mater. Chem. A* 4 (2016) 13223-13227.
- [13] G. Ali, A. Mehmood, H.Y. Ha, J. Kim, K.Y. Chung, *Sci. Rep.* 7 (2017) 40910.

- [14] Y. Liu, L.-Z. Fan, L. Jiao, *J. Mater. Chem. A* 5 (2017) 1698-1705.
- [15] B. Quan, S.-H. Yu, D.Y. Chung, A. Jin, J.H. Park, Y.-E. Sung, Y. Piao, *Scientific reports* 4 (2014) 5639.
- [16] Y. Zhou, Y. Leng, W. Zhou, J. Huang, M. Zhao, J. Zhan, C. Feng, Z. Tang, S. Chen, H. Liu, *Nano Energy* 16 (2015) 357-366.
- [17] H. Song, N. Li, H. Cui, C. Wang, *Nano Energy* 4 (2014) 81-87.
- [18] Q. Fan, W. Zhang, J. Duan, K. Hong, L. Xue, Y. Huang, *Electrochim. Acta* 174 (2015) 970-977.
- [19] D. Li, H. Chen, G. Liu, M. Wei, L.-x. Ding, S. Wang, H. Wang, *Carbon* 94 (2015) 888-894.
- [20] J. Xu, M. Wang, N.P. Wickramaratne, M. Jaroniec, S. Dou, L. Dai, *Adv. Mater.* 27 (2015) 2042-2048.
- [21] Y. Li, Z. Wang, L. Li, S. Peng, L. Zhang, M. Srinivasan, S. Ramakrishna, *Carbon* 99 (2016) 556-563.
- [22] S. Lee, M. Choun, Y. Ye, J. Lee, Y. Mun, E. Kang, J. Hwang, Y.-H. Lee, C.-H. Shin, S.-H. Moon, S.-K. Kim, E. Lee, J. Lee, *Angew. Chem.* 127 (2015) 9362-9366.
- [23] J. Park, J. Moon, C. Kim, J.H. Kang, E. Lim, J. Park, K.J. Lee, S.-H. Yu, J.-H. Seo, J. Lee, J. Heo, N. Tanaka, S.-P. Cho, J. Pyun, J. Cabana, B.H. Hong, Y.-E. Sung, *NPG Asia Mater.* 8 (2016) e272.
- [24] J. Yang, X. Zhou, D. Wu, X. Zhao, Z. Zhou, *Adv. Mater.* 29 (2017) 1604108.
- [25] L. Qie, W. Chen, X. Xiong, C. Hu, F. Zou, P. Hu, Y. Huang, *Adv. Sci.* 2 (2015) 1500195.
- [26] X. Deng, K. Xie, L. Li, W. Zhou, J. Sunarso, Z. Shao, *Carbon* 107 (2016) 67-73.

- [27] M. Choucair, P. Thordarson, J.A. Stride, *Nat. Nanotechnol.* 4 (2009) 30-33.
- [28] H. Wang, T. Maiyalagan, X. Wang, *ACS Catal.* 2 (2012) 781-794.
- [29] H.L. Poh, P. Šimek, Z. Sofer, M. Pumera, *ACS Nano* 7 (2013) 5262-5272.
- [30] D. Wei, Y. Liu, Y. Wang, H. Zhang, L. Huang, G. Yu, *Nano Lett.* 9 (2009) 1752-1758.
- [31] Y.-X. Wang, S.-L. Chou, H.-K. Liu, S.-X. Dou, *Carbon* 57 (2013) 202-208.
- [32] H. Hou, C.E. Banks, M. Jing, Y. Zhang, X. Ji, *Adv. Mater.* 27 (2015) 7861-7866.
- [33] S. Xin, Y.-X. Yin, Y.-G. Guo, L.-J. Wan, *Adv. Mater.* 26 (2014) 1261-1265.
- [34] D. Xu, C. Chen, J. Xie, B. Zhang, L. Miao, J. Cai, Y. Huang, L. Zhang, *Adv. Energy Mater.* 6 (2016) 1501929.
- [35] L. Fu, K. Tang, K. Song, P.A. van Aken, Y. Yu, J. Maier, *Nanoscale* 6 (2014) 1384-1389.
- [36] T.H. Hwang, D.S. Jung, J.-S. Kim, B.G. Kim, J.W. Choi, *Nano Lett.* 13 (2013) 4532-4538.
- [37] T. Chen, Y. Liu, L. Pan, T. Lu, Y. Yao, Z. Sun, D.H.C. Chua, Q. Chen, *J. Mater. Chem. A* 2 (2014) 4117-4121.
- [38] M.M. Rahman, I. Sultana, Z. Chen, M. Srikanth, L.H. Li, X.J. Dai, Y. Chen, *Nanoscale* 7 (2015) 13088-13095.
- [39] X. Xie, Z. Ao, D. Su, J. Zhang, G. Wang, *Adv. Funct. Mater.* 25 (2015) 1393-1403.
- [40] D. Su, H.-J. Ahn, G. Wang, *Chem. Commun.* 49 (2013) 3131-3133.

Chapter 3. SnS/C Nanocomposites as Sodium Ion Battery Anode Materials with high Capacity and superior Rate Capability

3.1 Introduction

In recent years, sodium-ion batteries (SIBs) have emerged as attractive alternatives to replace lithium-ion batteries (LIBs) for large-scale energy storage applications because sodium is much more abundant and inexpensive than lithium [1-7]. Since both lithium and sodium are alkali metals with one electron in their valence shells, there was the expectation that materials developed for LIBs could be directly applied to SIBs. However, it is much more challenging to identify promising anode materials for SIBs, compared to LIBs, because sodium has a higher equilibrium potential and a larger ionic size [8-10]. For example, while graphite, used as anode, played a key role in commercializing LIBs, it has been reported that intercalation of sodium ions into graphite is hindered, so that graphite delivers a much lower capacity when applied to SIB anodes [11-13].

Recently, there has been a great deal of effort focused on the search for suitable anode materials for SIBs. Although silicon has been intensively studied for LIB anodes, due to its exceptionally high theoretical capacity, the redox potential of silicon is too low for application in SIBs [8,14]. Instead, other alloy-type materials such as Sn-, Sb-, and Ge-based materials have been examined in

detail as high-capacity anodes for SIBs [15-25]. In addition, it has been reported that various transition metal oxides, sulfides and selenides can store sodium ions reversibly through intercalation and/or conversion reactions [26-37]. Furthermore, several approaches have been introduced to facilitate intercalation of sodium ions into graphite by using expanded graphite, and ether-based electrolytes [11,38-40]. However, these materials still have limitations such as low capacity, poor rate capability, rapid capacity fade and complex preparation process.

Herein, we report a simple preparation method for SnS/C nanocomposites, and their application to sodium-ion battery anodes. The grain size of SnS could reach about 10 nm, and SnS particles were well surrounded by carbon particles thereby increasing conductivity. The nanocomposites exhibited significantly enhanced electrochemical performance when compared to those of bare SnS electrodes. The nanocomposites delivered a reversible capacity of 480.0 mAh g⁻¹ with negligible capacity fade during 50 cycles at a current density of 100 mA g⁻¹. The composites also showed outstanding rate capabilities, delivering ~93% of their capacity when the current density was increased by a factor of ten (from 50 to 500 mA g⁻¹). Furthermore, the reaction mechanism of SnS/C nanocomposites was studied using ex-situ transmission electron microscopy (TEM), X-ray diffraction (XRD) and operando X-ray absorption near edge structure (XANES).

3.2. Experimental section

3.2.1 Preparation method of tin (II) sulfide/carbon nanocomposites

Tin (II) sulfide (Aldrich) and super P carbon were mixed in a weight ratio of 7:3, and the mixture was transferred to ball-milling container in an argon-filled glove box. Mechanical ball-milling was conducted with PULVERISETTE7 (Fritsch) at a speed of 500 rpm during 10 hrs.

3.2.2 Materials characterization

Field-emission scanning electron microscopy (FE-SEM) analysis was conducted with a SUPRA 55VP (Carl Zeiss). X-ray diffraction patterns were obtained using Bruker D-5005 with Cu α radiation. *Operando* XANES experiments were conducted at the F-3 station of Cornell High Energy Synchrotron Sources (CHESS). High-resolution transmission electron microscopy (HRTEM) images and corresponding selected area electron diffraction (SAED) were obtained using a FEI field-emission-gun (FEG) Tecnai F-20 operated at 200 kV.

3.2.3 Electrochemical Characterization

A slurry, composed of 70 wt.% of active material, 15 wt.% of super P carbon and 15 wt.% of poly(acrylic acid) in N-methyl-2-pyrrolidinone solvent, was coated on the current collector. The electrodes were subsequently vacuum dried in an oven overnight at 120 °C. The loading mass of active material on electrode is about 1.4 mg cm⁻². The coin cells (CR-2032) were assembled in an argon-filled

glove box with sodium metal as both counter and reference electrodes. A glass fiber filter (GF/C,Whatman) was used as separator. 1.0 M NaClO₄ in ethylene carbonate (EC)/propylene carbonate (PC) (1:1 by volume) with 5 wt.% fluoroethylene carbonate (FEC) as additive was used as the electrolyte. Coin cells were tested on BT-2000 (Arbin Instruments) and WBCS3000 cyclers (WanA Tech) over a voltage range from 0.01 V to 3.0 V (vs. Na⁺/Na).

3.3 Results and discussion

3.3.1 Materials characterization of bare SnS and SnS/C nanocomposites

Figure 3.1a presents X-ray diffraction (XRD) patterns of bare SnS and ball-milled SnS/C composites. XRD peaks of bare SnS powder are well matched with values of SnS reference card (JCPDS No. 14-0620, orthorhombic structure, $a=4.33$, $b=11.19$ and $c=3.98$) without any impurity peaks. The (040) peak of bare SnS is overwhelmingly strong compared to other peaks, which indicates that SnS layers are preferentially stacked to the [010] direction (Figure 3.2b). XRD peaks of SnS/C composites are much broader than that of bare SnS, indicating that the grain size of SnS is even smaller. The calculated grain size of ball-milled SnS, by the Scherrer equation is about 10 nm. It is worthwhile to note that intensities of the (040) and (080) peaks decrease more significantly than other peaks after ball-milling. This suggests that layers of SnS are more easily broken in [010] direction than others during ball-milling process, and SnS particles after ball-milling might have much less two-dimensional (2D) characteristic (low aspect ratio) as shown in Figure 4.2. It is worth to note that obtaining nanosized material (<100 nm) using ball-milling is difficult in general, but intrinsically bare SnS has two-dimensional (2D) character with preferential direction, and thickness in the other direction is small. Therefore, small-sized SnS particles can be obtained simply using ball-milling, even size can reach to about 10 nm. XANES spectrum of SnS/C nanocomposites is overlapped with that of bare SnS, indicating that no phase transition (reduction/oxidation) was occurred during ball-milling process. (Figure 3.3)

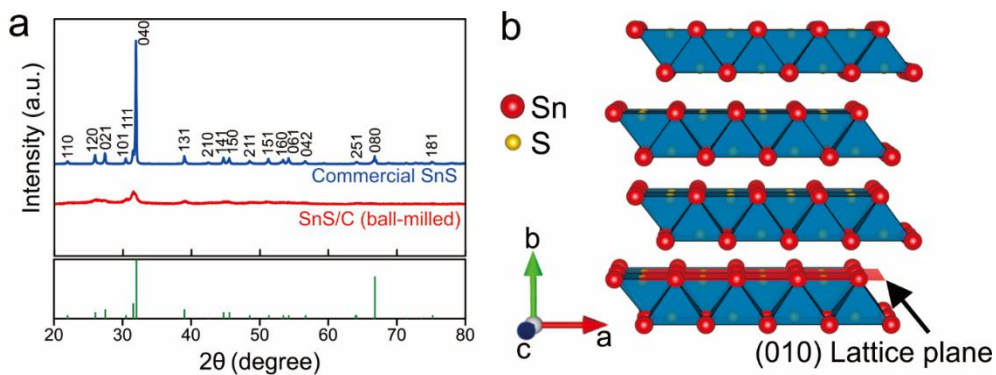


Figure 3. 1 XRD patterns of (a) bare SnS and SnS/C nanocomposites (top) and SnS from JCPDS No. 14-0620 (bottom). (b) Crystal structure of SnS along the [001] direction (*c*-axis direction).

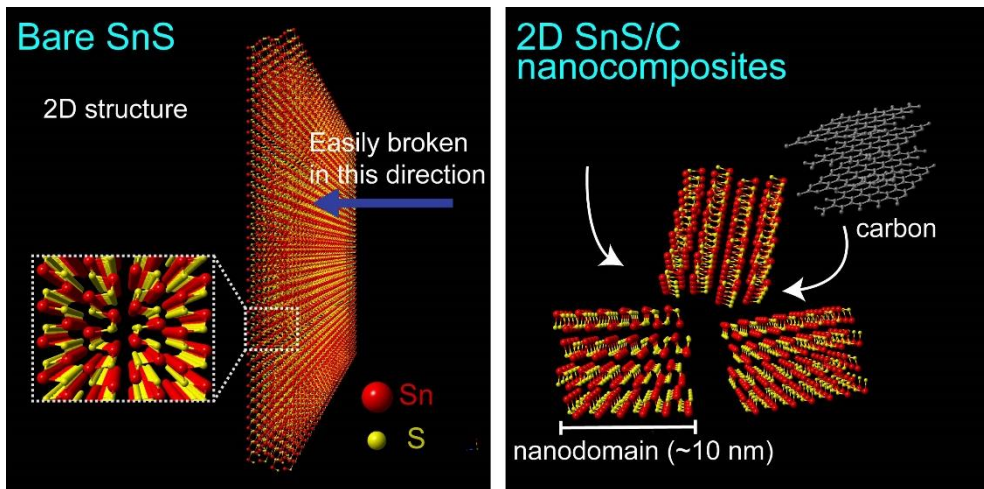


Figure 3. 2 Schematic illustration of mophology of (a) bare SnS and (b) SnS/C nanocomposites.

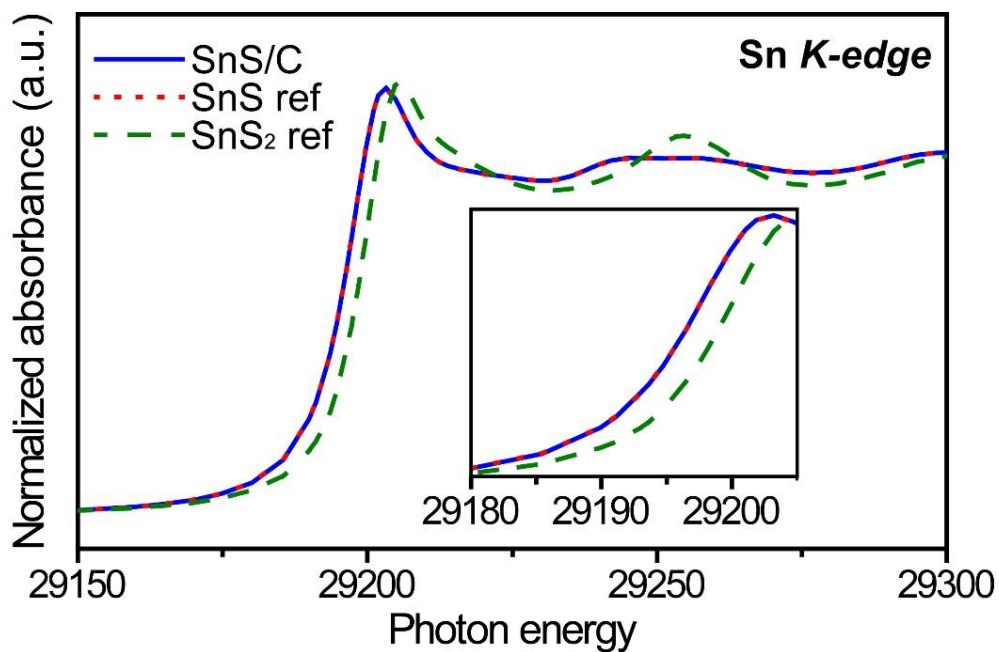


Figure 3. 3 XANES spectra of SnS/C nanocomposites (blue line), commercial SnS (red dots) and SnS₂ (green dash).

In scanning electron microscopy (SEM) images of bare SnS (Figure 3.4a and 3.4 b), several micron-sized SnS layers with thin (~50 nm) thickness are observed. Based on the FFT, the most prominently observed interplanar distance is 0.29 nm for (101) planes at top view of SnS sheet as can be seen in transmission electron microscopy (TEM) images (Figure 3.4a and 3.4b), supporting that layers are preferentially grown along the [010] direction. After ball-milling, the SnS particles have nonhomogeneous size distribution, from ~50 nm to 1 μm , and they are well covered by carbon particles (Figure 3.3 c, 3.3d, and 3.4 c). In the HRTEM and STEM images of SnS/C nanocomposites (Figure 3.4d, 3.5, 3.6 and 3.7), it can be observed that they still have 2D characteristic, and the typical grain size is ~10 nm, which is in good agreement with value calculated from the XRD results presented above.

3.3.2 Electrochemical properties of bare SnS and SnS/C nano composites

The electrochemical properties of bare SnS and SnS/C nanocomposites were evaluated as anode materials for SIBs. The cells were galvanostatically discharged and charged at a current density of 100 mA g^{-1} in the voltage range of 0.01-3.0 V (vs. Na^+/Na) (Figure 3.8 and Figure 3.9). For bare SnS, the initial sodiation and desodiation capacities were 740.2 and 592.5 mAh g^{-1} , respectively (Fig. 3.8a). The large plateau started at about 0.85 V during the initial sodiation process, and starting potential moved to higher at subsequent cycles. Similarly, the strong peak at about 0.52 V at the first reduction disappeared, and two separate peaks at higher potential (0.97 and 0.67 V) appeared from the second

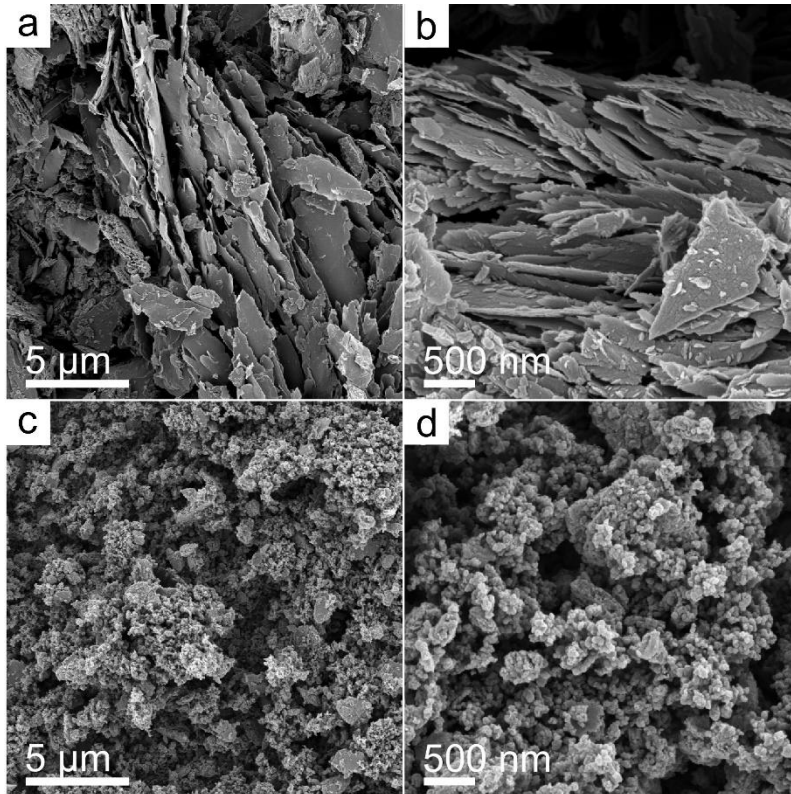


Figure 3. 4 SEM images of (a-b) bare SnS, (c-d) SnS/C nanocomposites.

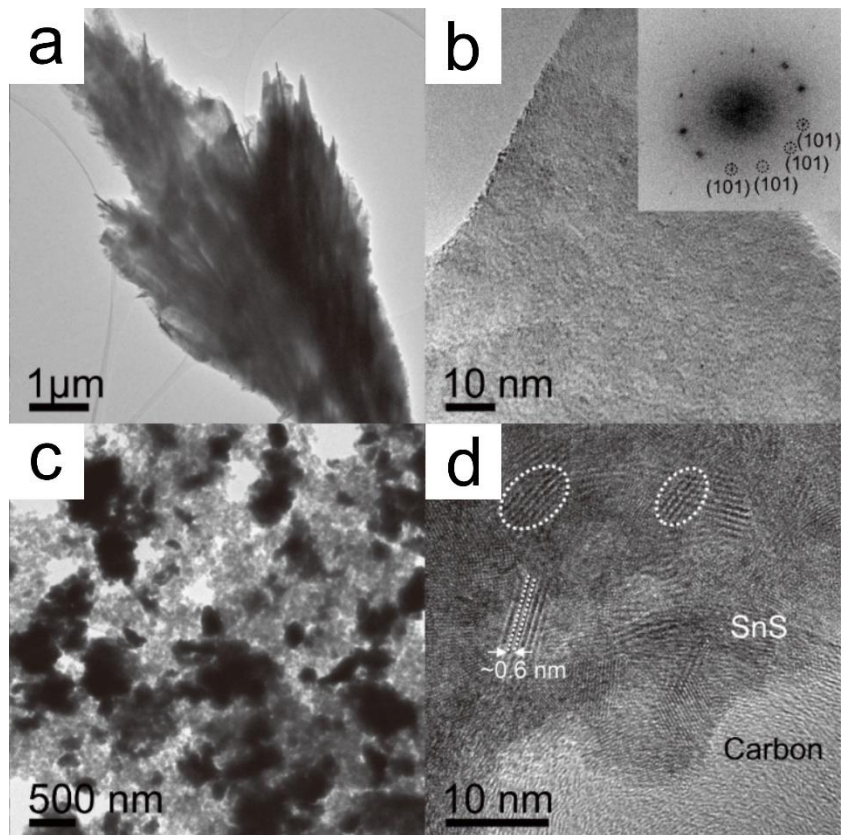


Figure 3. 5 TEM images of (a-b) bare SnS (inset of c shows fast Fourier transform (FFT) image of whole region in c.), (c-d) SnS/C nanocomposites.

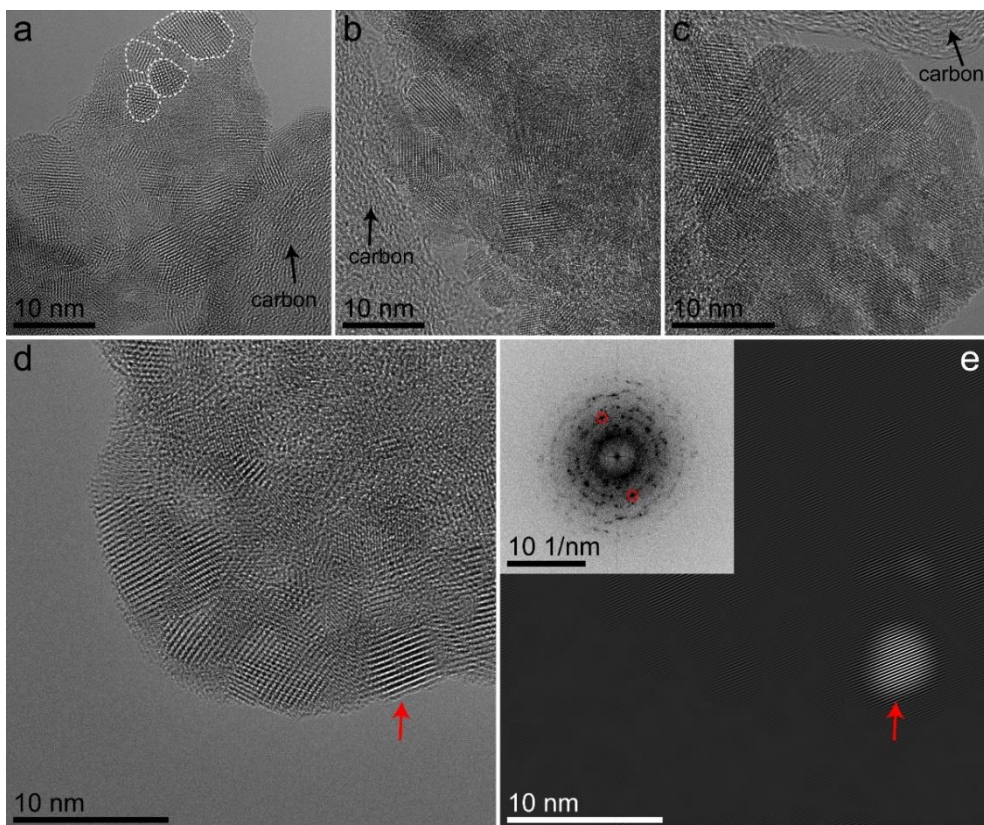


Figure 3. 6 (a)-(d) High-resolution TEM images of SnS/C nanocomposites, and (e) inverse fast Fourier transformed (FFT) image from the region circled by red in inset. Inset shows FFT image of (d).

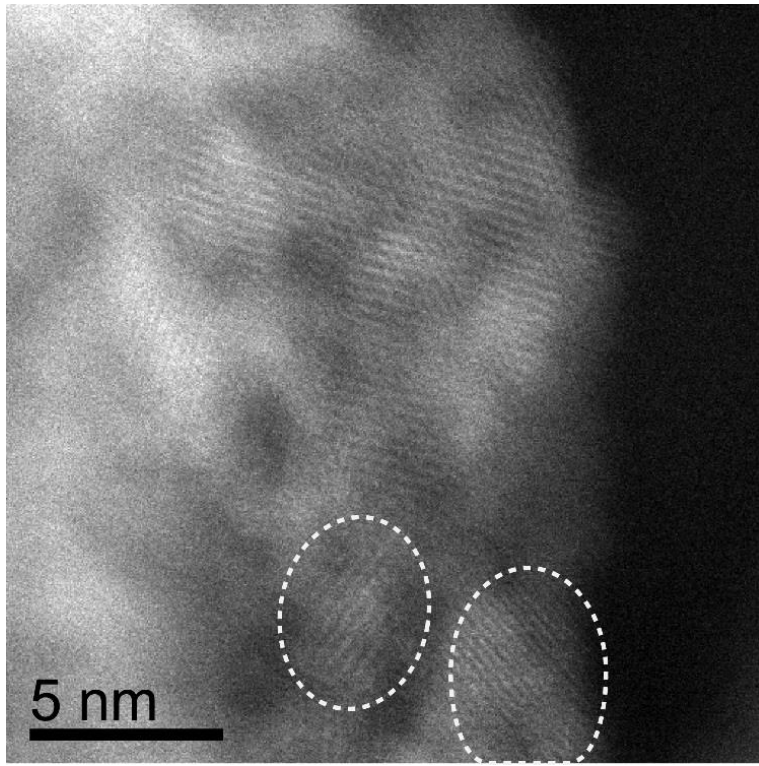


Figure 3.7 STEM image of SnS/C nanocomposites.

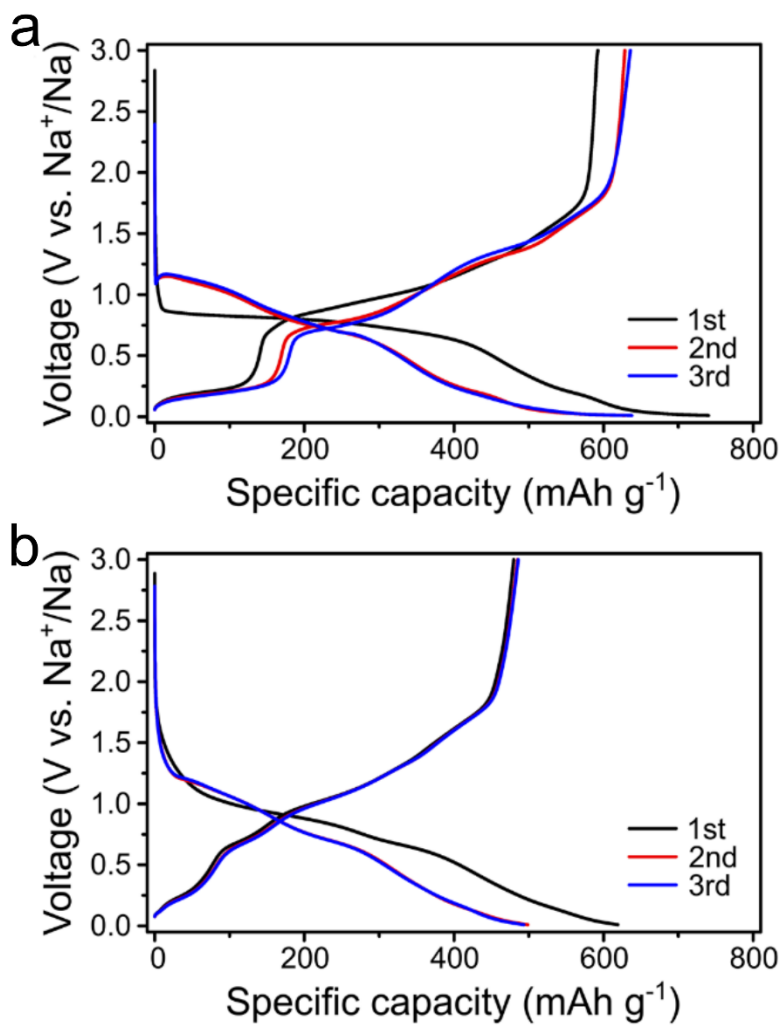


Figure 3. 8 Voltage profiles of (a) bare SnS and (b) SnS/C nanocomposites at a current density of 100 mA g⁻¹.

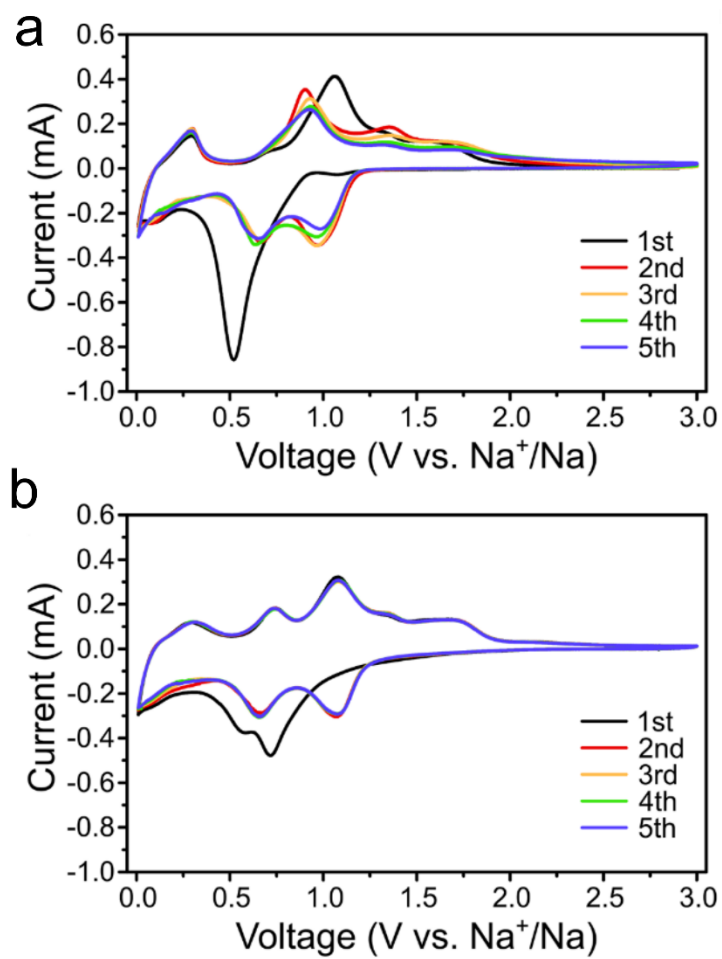


Figure 3. 9 Cyclic voltammograms of (a) bare SnS and (b) SnS/C nanocomposites at a scan rate of 0.1 mV s⁻¹.

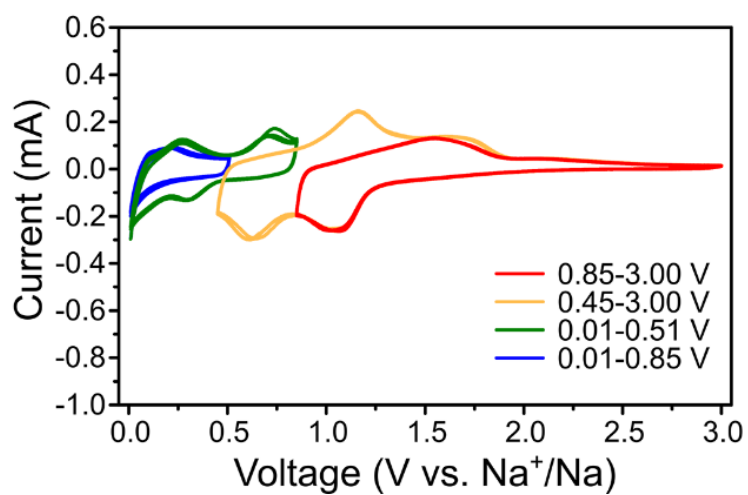


Figure 3. 10 Cyclic voltammograms of SnS/C nanocomposites at a scan rate of 0.1 mV s^{-1} with different cut off voltage ranges.

cycle in cyclic voltammograms (CVs) (Figure 3.9a). This activation process during the initial discharge is typically observed phenomenon in conversion reaction based materials in LIBs and SIBs, because the materials have very small domain size after the initial discharge [41-43]. Figure 3.8b and 3.9b present voltage profiles and CVs of SnS/C nanocomposites, respectively. In Figure 3.8c, the first and second sodiation profiles are still different, but much more similar compared to two profiles shown in Figure 3.8a. It could be understood that the grain size of initial SnS/C nanocomposites is much smaller (~10 nm) than that of bare SnS, so the difference before and after the first cycle in SnS/C nanocomposites is less significant. In Figure 3.9b, many peaks are observed during reduction and oxidation processes, but it is complicated to match the redox pairs. In order to understand which reduction and anodic peaks are pair, we performed cyclic voltammetry with different cut-off voltage after fully sodiation (Figure 3.10). From this, we can clearly define the redox pairs: the cathodic peaks at 1.08, 0.65, 0.30, and 0.01 V and anodic peaks at 1.70, 1.07, 0.74, and 0.28, are pairs, respectively. Comparing the CVs of bare SnS and SnS/C nanocomposites, it is worth to comment two. Firstly, although both anodic and cathodic peaks slowly decreased during the initial five cycles, especially at high potential (>0.8 V) in Figure 3.9b, CVs of SnS/C nanocomposites are entirely overlapped (Figure 3.9b), showing enhanced stability. Secondly, the peaks of SnS/C nanocomposites are shown at higher and lower potential than those of bare SnS during reduction and oxidation process, respectively, indicating improved reaction kinetic of SnS/C nanocomposites. Figure 3.11 presents cycle

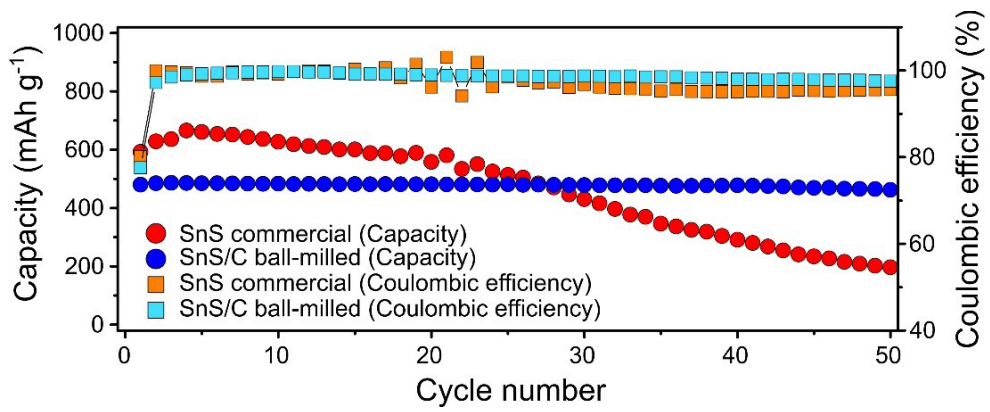


Figure 3. 11 Cycle performance of bare SnS and SnS/C nanocomposites at a current density of 100 mA g⁻¹.

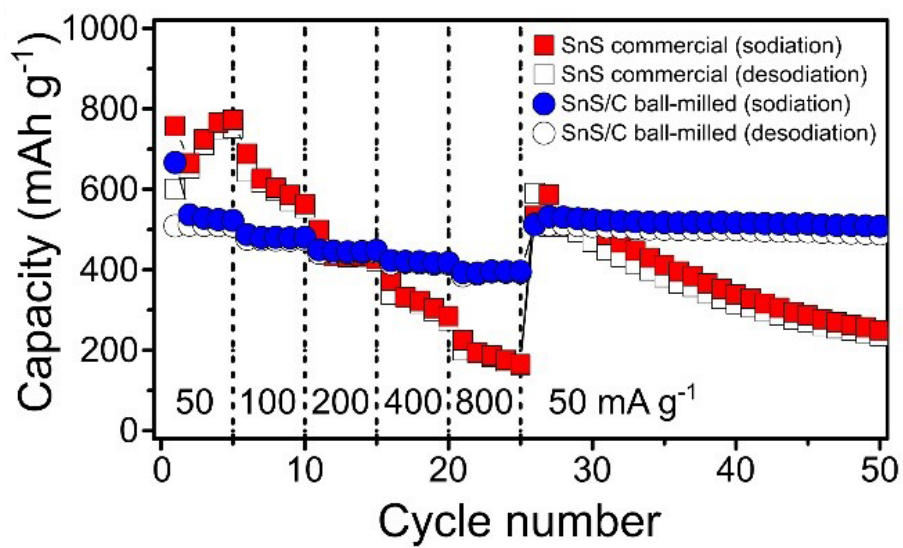


Figure 3. 12 Rate properties of bare SnS and SnS/C nanocomposites at various current densities.

performance of bare SnS and SnS/C nanocomposites. The initial desodiation capacity of SnS/C composites is 480.0 mAh g⁻¹, which is 685.7 mAh g⁻¹ when calculated based on weight of SnS only. The capacity of bare SnS electrode decreases on weight of SnS only. The capacity of bare SnS electrode decreases continuously during 50 cycles, but the cycle retention of SnS/C nanocomposites is much higher, which reaches 96.3% during 50 cycles.

Rate properties of bare SnS and SnS/C nanocomposite were evaluated by varying the current density stepwise from 50 through 800 mA g⁻¹ (Figure 3.12). When current density increased, the capacity of bare SnS decreased significantly. At high current density of 800 mA g⁻¹, bare SnS has low capacity (<200 mAh g⁻¹), whereas SnS/C nanocomposites still delivered high capacity of about 400 mAh g⁻¹. In addition, SnS/C nanocomposites showed stable cycling even at a current density of 800 mA g⁻¹, it is excellent property especially when we consider this current density enables two full sodiation or desodiation in one hour. The current density was changed back to 50 mA g⁻¹ after increasing to 800 mA g⁻¹, the capacity of SnS/C nanocomposites also recovered to the initial one, indicating that there was no structural damage during high rate cycling. The voltage profiles at the fifth cycle of each step were plotted in Figure 3.13a and 3.13b for bare SnS and SnS/C nanocomposites, respectively. In the voltage profiles of bare SnS (Figure 3.14b), large overpotential can be observed and reaction plateaus are unclear at high current density. On the contrary, the much smaller overpotential is observed in the voltage profiles of SnS/C nanocomposites, and reaction plateaus are also clearly seen at current density of

800 mA g⁻¹. Figure 3.14 shows cycle performance of SnS/C nanocomposites at various current density. The first reversible capacities are 488.2 and 441.2 at current density of 50 and 500 mA g⁻¹, indicating that the relative capacity reaches 90.4% even the current density increases ten times. In addition, SnS/C composites exhibited excellent cyclic stability during 50 cycles at all current densities from 50 to 500 mA g⁻¹. In particular, the capacity retention is 98.7% at 500 mA g⁻¹, which is the much higher compared to those in other reported anode materials [44-47]. We also prepared SnS/C nanocomposites using mesoporous carbon (CMK) instead of super P carbon as a supporting data, which also showed much improved cyclic stability and rate properties (Figure 3.15 and Figure 3.16). This confirms that SnS can have excellent electrochemical properties when they are ball milled with carbon with no dependence on kinds of carbon, so SnS/C nanocomposites are very attractive not only in aspect of battery performance but also practical aspect.

3.3.3 Reaction mechanism of bare SnS and SnS/C nanocomposites

In order to clarify the reaction mechanism of SnS/C composite, *ex-situ* XRD and *operando* X-ray absorption near edge structure (XANES) analyses were performed in Figure 3.17 and Figure 3.18. The broad XRD peak from SnS started to weaken during the initial sodiation, and disappeared at 0.67 V. At the same time, the peaks related to Sn metal appeared, indicating that conversion reaction of SnS occurred to form Sn metal and amorphous sodium sulfide. At fully sodiation state (0.01 V), Sn metal peaks can be seen in XRD patterns.

Additionally, weak electron diffraction patterns corresponding to Sn metal and $\text{Na}_{15}\text{Sn}_4$ phase are observed in SAED pattern at the fully sodiation state (0.01 V) (Figure 3.18b). This suggested that some of Sn metal clusters reacted with sodium ion to form $\text{Na}_{15}\text{Sn}_4$ through alloy reactions, but it is difficult to detect diffraction patterns of Na-Sn alloy phases because of their small particle size and low crystallinity [48, 49]. During desodiation, XRD peaks from Sn totally disappeared, and no other patterns from active material are observed at fully desodiation state (3.0 V). Similarly, only carbon electron diffraction patterns are observed at fully desodiation state (Figure 3.18d). In XANES spectra, the peak height continuously decreased during sodiation (Figure 3.17), reached to that of Sn reference metal at 0.48 V, and further decreased until fully discharged. This means that conversion reaction of SnS to Sn metal completed around 0.5 V and further sodiation process into Sn metal occurred at lower potential. During desodiation (Figure 3.17), the peak height continuously increased, reached to that of Sn reference metal at 1.00 V, and kept further increasing, indicating Na-Sn alloy oxidized to Sn metal, and continuously changed to SnS above 1.0 V. It is worthwhile to note that XANES spectra of SnS/C composites before test, and after 1st and 2nd cycle at charged state are totally overlapped, indicating that the reaction of SnS/C nanocomposites is highly reversible although the reactions go through multiple steps involving conversion and alloying reactions.(Figure 3.20) When compared with tin oxide-based materials, which also go through both conversion and alloying reaction similarly to tin sulfides, their conversion reactions are known to be irreversible [50, 51].

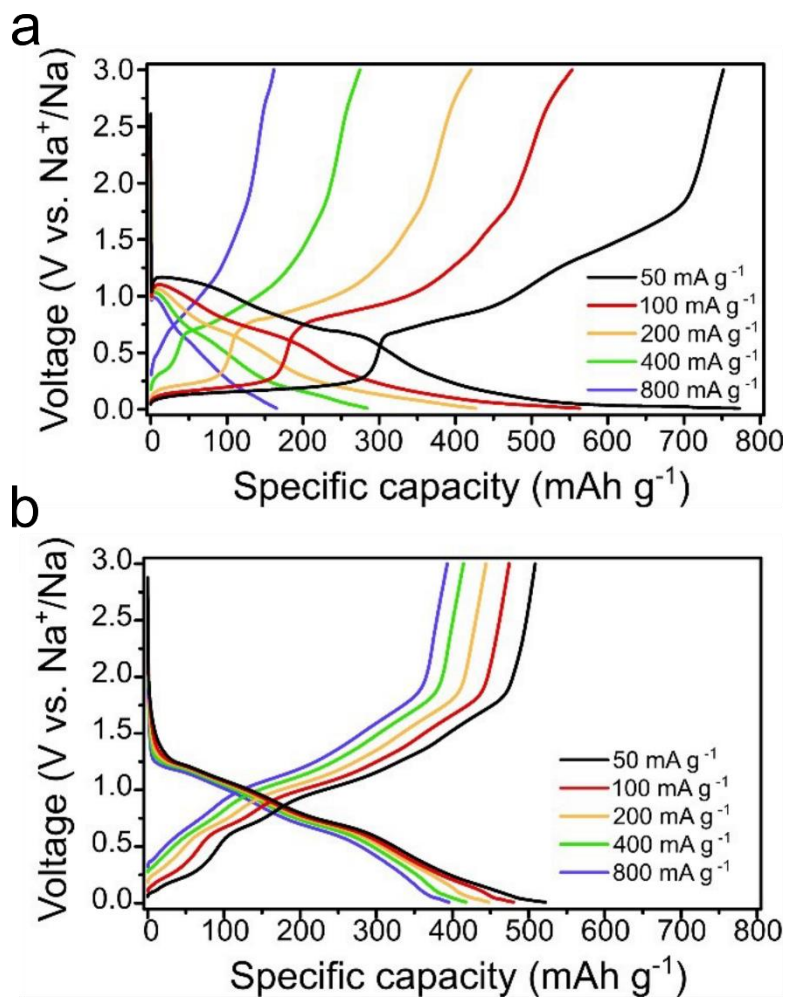


Figure 3. 13 Voltage profiles of (b) bare SnS and (c) SnS/C nanocomposites at various current densities.

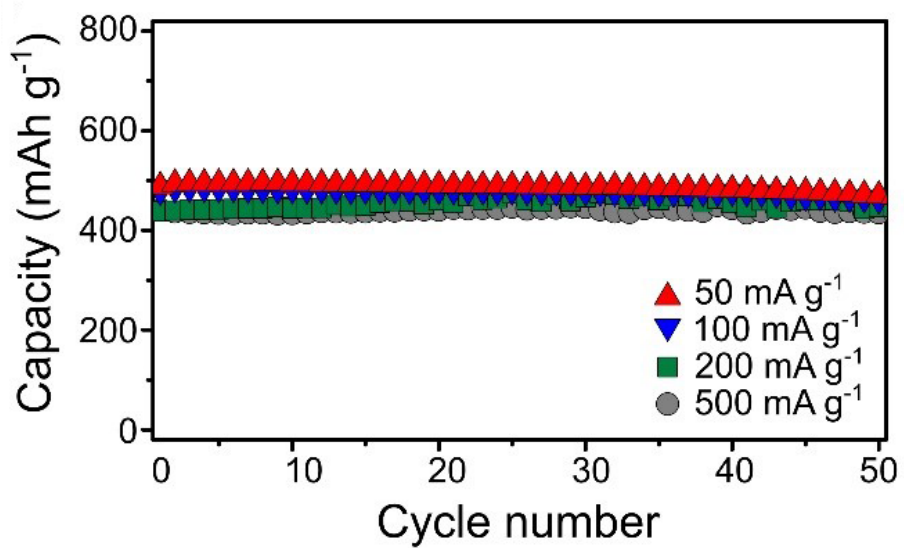


Figure 3. 14 Cycle performance of 2D SnS/C nanocomposites at various current densities.

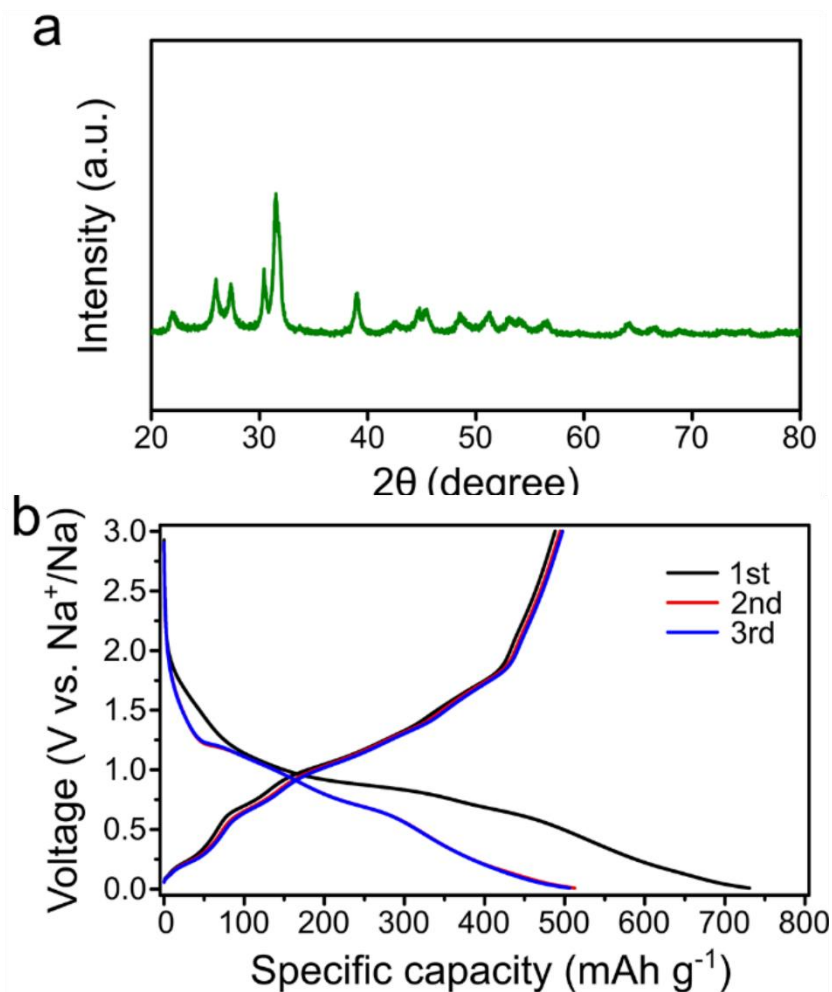


Figure 3. 15 (a) XRD patterns of tin sulfide/mesoporous carbon (CMK) composites prepared by ball milling method. (b) Voltage profiles of tin sulfide/mesoporous carbon (CMK) composites at a current density of 100 mA g^{-1}

1.

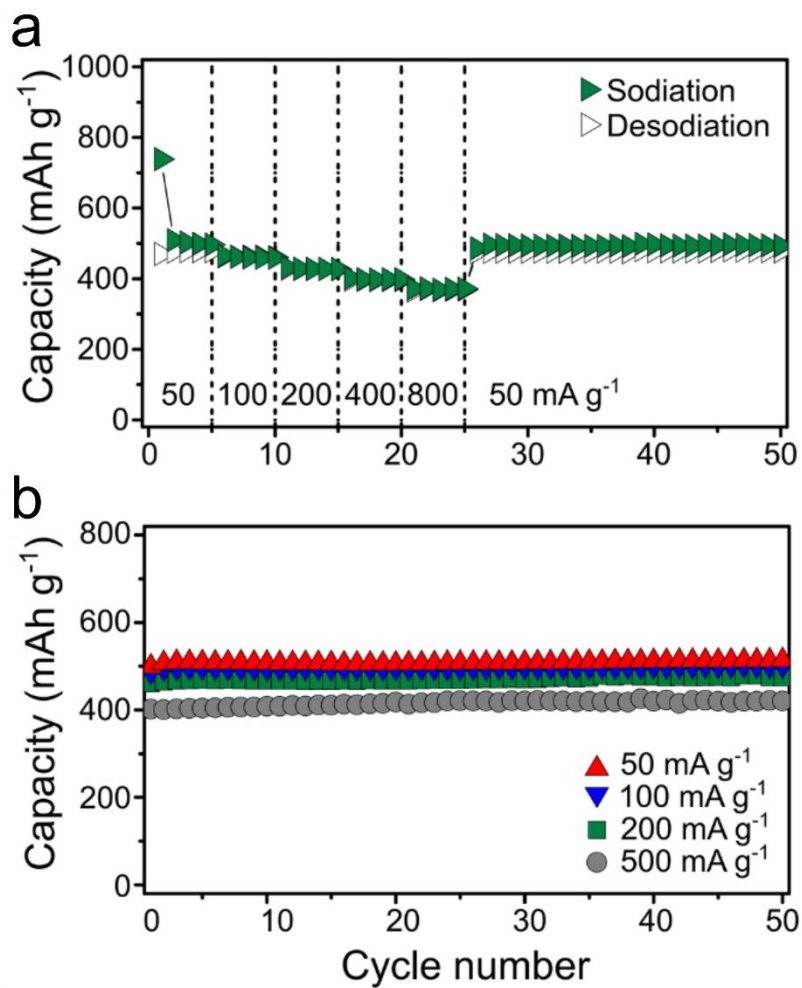


Figure 3. 16 (a) Rate properties of tin sulfide/mesoporous carbon (CMK) composites. (b) Cycle performance of tin sulfide/mesoporous carbon (CMK) composites at various current densities.

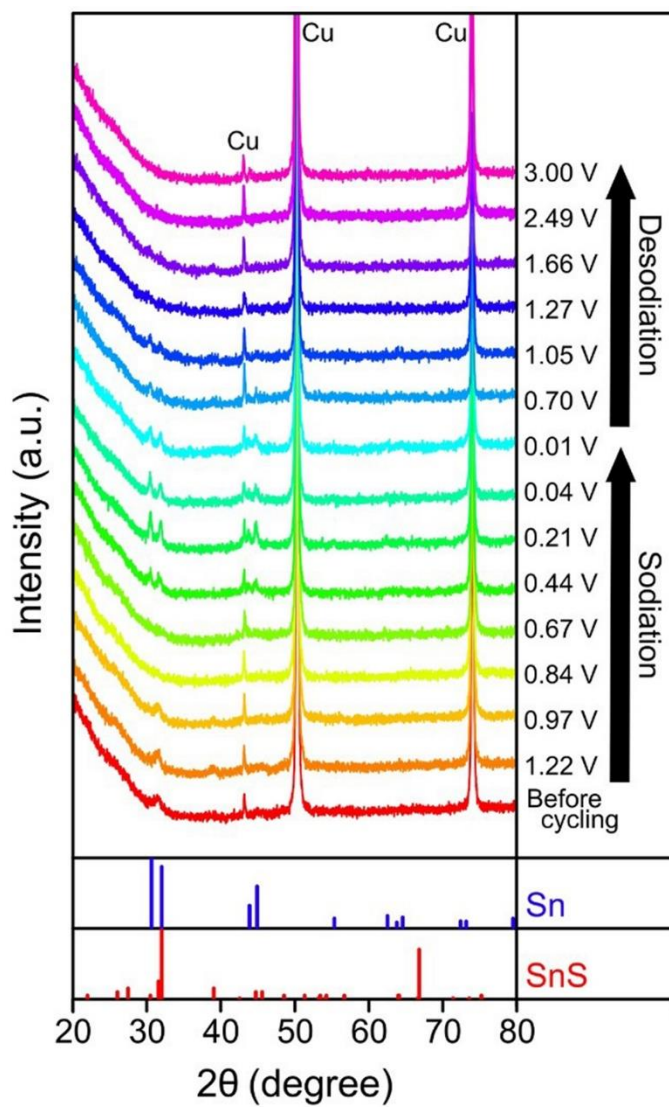


Figure 3. 17 *Ex-situ* XRD patterns during the first sodiation and desodiation process.

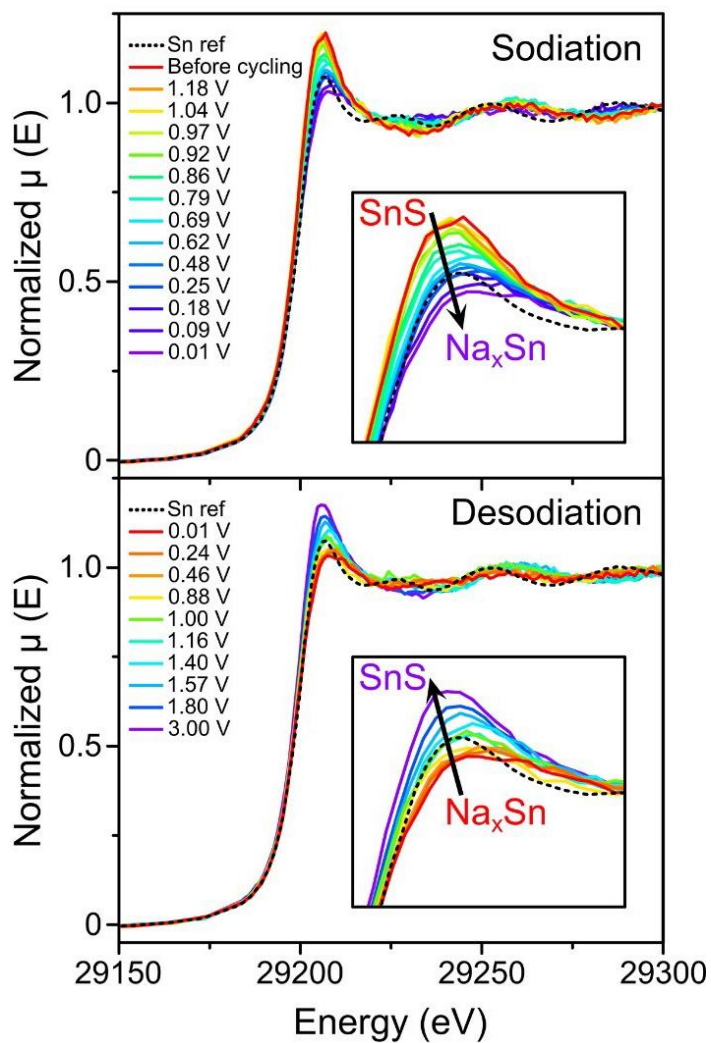


Figure 3. 18 (a) *operando* XANES spectra of SnS/C nanocomposites at Sn K edge during the first sodiation and desodiation process.

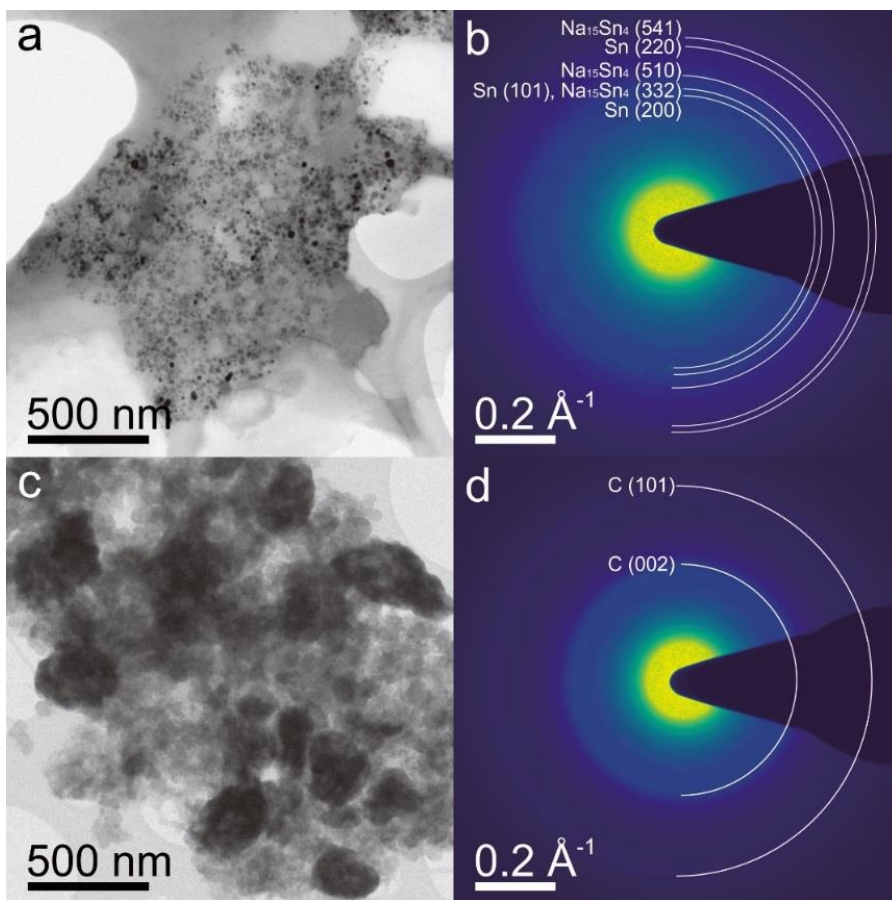


Figure 3. 19 (a) TEM image and (b) SAED pattern of SnS/C nanocomposites at fully sodiated state (0.01 V). (c) TEM image and (d) SAED pattern of SnS/C nanocomposites at fully desodiated state (3.0 V).

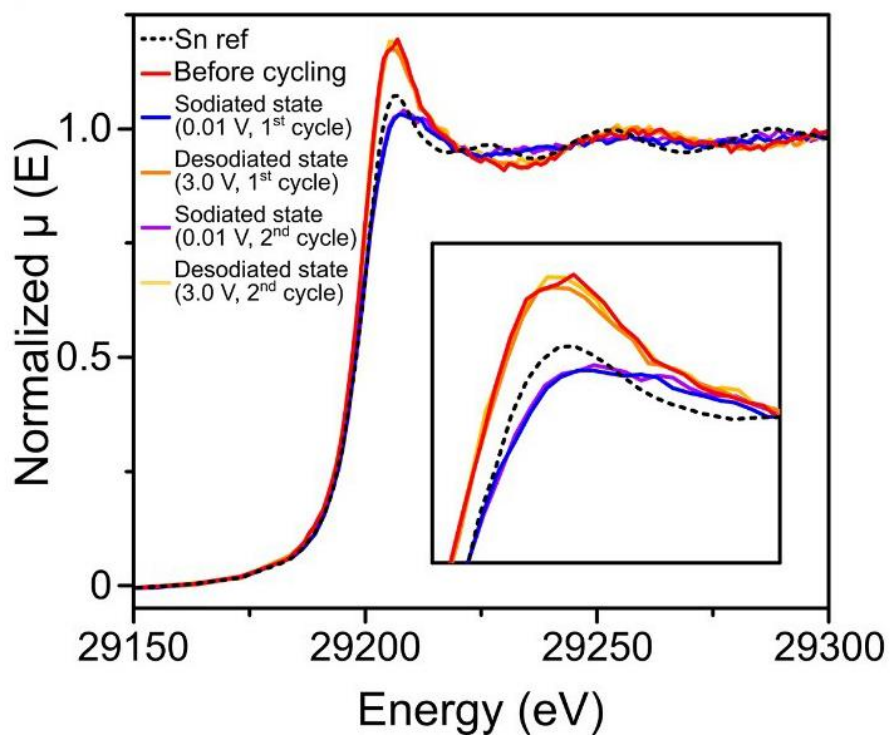


Figure 3. 20 XANES spectra of SnS/C nanocomposites at Sn K edge composites before battery test, after the first and second sodiation and desodiation.

3.4 Conclusions

SnS/C nanocomposites were obtained through a practical and economical top-down approach. The unique structural properties of SnS enable to reach small nanodomain of about 10 nm using ball-milling process. The SnS/C nanocomposites exhibited superior electrochemical performance, compared to bare SnS, for sodium ion batteries. The SnS/C nanocomposites delivered a high desodiation capacity of about 480 mAh g⁻¹ (about 686 mAh g⁻¹ when calculated based on the weight of SnS alone) at a current density of 100 mAh g⁻¹ through multiple reaction steps including conversion and alloying reactions. They also showed excellent cycling stability at various current densities, with more than 90% of its capacity delivered when the current increased from 50 to 500 mA g⁻¹. The sodiation/desodiation reaction mechanism of SnS/C composites was studied by *ex-situ* TEM, XRD and operando XANES analyses. The reactions of SnS/C nanocomposites were remarkably reversible, as established by cyclic voltammetry and operando XANES analysis. We believe that the approach that we have used in this study, for the preparation of SnS/C nanocomposites, will provide valuable insights into developing practical and promising anode materials for sodium-ion batteries.

3.5 References

- [1] M. D. Slater, D. Kim, E. Lee, C. S. Johnson, *Adv. Funct. Mater.* 23 (2013) 947-958.
- [2] H. Pan, Y. -S. Hu, L. Chen, *Energy Environ. Sci.* 6 (2013) 2338-2360.
- [3] N. Yabuuchi, K. Kubota, M. Dahbi, S. Komaba, *Chem. Rev.* 114 (2014) 11636-11682.
- [4] S. -W. Kim, D. -H. Seo, X. Ma, G. Ceder, K. Kang, *Adv. Energy. Mater.* 2 (2012) 710-721.
- [5] Y. Wang, X. Yu, S. Xu, J. Bai, R. Xiao, Y. -S. Hu, H. Li, X. -Q. Yang, L. Chen, X. Huang, *Nat. Commun.* 4 (2013) 2365.
- [6] J.-Y. Hwang, S.-T. Myung and Y.-K. Sun, *Chem. Soc. Rev.* 46 (2017) 3529.
- [7] K. Kubota and S. Komaba, *J. Electrochem. Soc.* 162 (2015) A2538.
- [8] Y. Kim, K. -H. Ha, S. M. Oh, K. T. Lee, High-Capacity Anode Materials for Sodium-Ion Batteries, *Chem. Eur. J.* 20 (2014) 11980-11992.
- [9] J. Qian, X. Wu, Y. Cao, X. Ai, H. Yang, *Angew. Chem.* 125 (2015) 4731-4734.
- [10] M. Dahbi, N. Yabbuchi, K. Kubota, K. Tokiwa, S. Komaba, *Phys. Chem. Chem. Phys.* 16 (2014) 15007-15028.
- [11] Y. Wen, K. He, Y. Zhu, F. Han, Y. Xu, I. Matsuda, Y. Ishii, J. Cumings, C. Wang, *Nat. Commun.* 5 (2014) 4033.
- [12] S. Komaba, W. Murata, T. Ishikawa, N. Yabuuchi, T. Ozeki, T. Nakayama, A. Ogata, K. Gotch, K. Fujiwara, *Adv. Funct. Mater.* 21 (2011) 3859-3867.

- [13] E. Irisarri, A. Ponrouch, M. R. Palacin, *J. Electrochem. Soc.* 162 (2015) A2476-A2482.
- [14] V. L. Chevrier, G. Ceder, *J. Electrochem. Soc.* 158 (2011) A1011-A1014.
- [15] L. D. Ellis, T. D. Hatchard, M. N. Obrovac, *J. Electrochem. Soc.* 159 (2012) A1801-A1805.
- [16] Y. Liu, N. Zhang, L. Jiao, Z. Tao, J. Chen, *Adv. Funct. Mater.* 25 (2015) 214-220.
- [17] Z. Li, J. Ding, D. Mitlin, *Acc. Chem. Res.* 48 (2015) 1657-1665.
- [18] B. Zhang, G. Rousse, D. Foix, R. Dugas, D. A. D. Corte, J. –M. Tarascon, *Adv. Mater.* 28 (2016) 9824-9830.
- [19] A. Darwiche, C. Marino, M. T. Sougrati, B. Fraise, L. Stievano, L. Monconduit, *J. Am. Chem. Soc.* 134 (2012) 20805-20811.
- [20] M. He, K. Kravchyk, M. Walter, M. V. Kovalenko, *Nano Lett.* 14 (2014) 1255-1262.
- [21] L. Hu, X. Zhu, Y. Du, Y. Li, X. Zhou, J. Bao, *Chem. Mater.* 27 (2015) 8138-8145.
- [22] L. Baggetto, J. K. Keum, J. F. Browning, G. M. Veith, *Electrochem. Commun.* 34 (2013) 41-44.
- [23] Z. Li, X. Tan, P. Li, P. Kalisvaart, M. T. Janish, W. M. Mook, E. J. Lubber, K. L. Jungjohann, C. B. Carter, D. Mitlin, *Nano Lett.* 15 (2015) 6339-6348.
- [24] S. H. Choi and Y. C. Kang, *Nano Res.* 8 (2015) 1595.
- [25] L. Wu, H. Lu, L. Xiao, J. Qian, X. Ai, H. Yang and Y. Cao, *J. Mater. Chem.* A 2 (2014) 16424.

- [26] Y. Jiang, M. Hu, D. Zhang, T. Yuan, W. Sun, B. Xu, M. Yan, *Nano Energy* 5 (2014) 60-66.
- [27] Y. Liu, N. Zhang, C. Yu, L. Jiao, J. Chen, *Nano Lett.* 16 (2016) 3321-3328.
- [28] K. He, F. Lin, Y. Zhu, X. Yu, J. Li, R. Lin, D. Nordlund, T. -C. Weng, R. M. Richards, X. -Q. Yang, M. M. Doeff, E. A. Stach, Y. Mo, H. L. Xin, D. Su, *Nano Lett.* 15 (2015) 5755-5763.
- [29] Y. Denis, P. V. Prikhodchenko, C. W. Mason, S. K. Batabyal, J. Gun, S. Sladkevich, A. G. Medvedev, O. Lev, *Nat. Commun.* 4 (2013) 2922.
- [30] T. Zhou, W. K. Pang, C. Zhang, J. Yang, Z. Chen, H. K. Liu, Z. Guo, *ACS Nano* 8 (2014) 8323-8333.
- [31] L David, R. Bhandavat, G. Singh, *ACS Nano* 8 (2014)1759-1770.
- [32] Y. -L. Ding, P. Kopold, K. Hahn, P. A. v. Aken, J. Maier, Y. Yu, *Adv. Mater.* 28 (2016) 7774-7782.
- [33] Y. Xiao, S. H. Lee and Y.-K. Sun, *Adv. Energy Mater.* 7 (2017) 1601329.
- [34] Z. Hu, Q. Liu, S.-L. Chou and S.-X. Dou, *Adv. Mater.* 29 (2017) 1700606.
- [35] P. Ge, C. Zhang, H. Hou, B. Wu, L. Zhou, S. Li, T. Wu, J. Hu, L. Mai and X. Ji, *Nano Energy* 48 (2018) 617.
- [36] M. Wan, R. Zeng, K. Chen, G. Liu, W. Chen, L. Wang, N. Zhang, L. Xue, W. Zhang and Y. Huang, *Energy Storage Mater.* 10 (2018) 114.
- [37] P. Ge, H. Hou, X. Ji, Z. Huang, S. Li and L. Huang, *Mater. Chem. Phys.* 203 (2018) 185.
- [38] B. Jache, P. Adelhelm, *Angew. Chem. Int. Ed.* 53 (2014) 10169-10173.

- [39] A. P. Cohn, K. Share, R. Carter, L. Oakes, C. L. Pint, *Nano Lett.* 16 (2016) 543-548.
- [40] H. Kim, J. Hong, G. Yoon, H. Kim, K. -Y. Park, M. -S. Park, W. -S. Yoon, K. Kang, *Energy Environ. Sci.* 8 (2015) 2963-2969.
- [41] S. -H. Yu, S. H. Lee, D. J. Lee, Y. -E. Sung, T. Hyeon, *Small* 16 (2016) 2146-2172.
- [42] M. A. Lowe, J. Gao, H. D. Abruña, *J. Mater. Chem.* 1 (2013) 2094-2103.
- [43] F. Klein, B. Jache, A. Bhide, P. Adelhelm, *Phys. Chem. Chem. Phys.* 15 (2013) 15876-15887.
- [44] Y. M. Lin, P. R. Abel, A. Gupta, J. B. Goodenough, A. Heller, C. B. Mullins, *ACS Appl. Mater. Interfaces* 5 (2013) 8273-8277.
- [45] P. K. Dutta, U. K. Sen, S. Mitra, *RSC Adv.* 4 (2014) 43155-43159.
- [46] Y. Zhu, X. Han, Y. Xu, Y. Liu, S. Zheng, K. Xu, L. Hu, C. Wang, *ACS Nano* 7 (2013) 6378-6386.
- [47] Z. Jian, B. Zhao, P. Liu, F. Li, M. Zheng, M. Chen, Y. Shi, H. Zhou, *Chem. Commun* 50 (2014) 1215-1217.
- [48] J. W. Wang, X. H. Liu, S. X. Mao, J. Y. Huang, *Nano Lett.* 12 (2012) 5897-5902.
- [49] C. Ma, J. Xu, J. Alvarado, B. Qu, J. Somerville, J. Y. Lee, Y. S. Meng , *Chem. Mater.* 27 (2015) 5633-5640.
- [50] I. A. Courtney, J. R. Dahn, *J. Electrochem. Soc.* 144 (1997) 2045-2052.
- [51] M. Gu, A. Kushima, Y. Shao, J. -G. Zhang, J. Liu, N. D. Browning, J. Li, C. Wang, *Nano Lett.* 13 (2013) 5203-5211.

국 문 초 록

리튬 이온 전지는 지난 수십 년 동안 청정 에너지에 대한 요구로 인해 휴대용 전자 장치 및 전기 자동차와 같은 여러 분야에 가장 널리 사용되는 전원으로 여겨졌다. 그러나 리튬 자원은 전 세계적으로 제한적이고 불균일하게 분포되어 있으므로 리튬 이온 전지의 수요가 증가함에 따라 자재 비용이 증가하고 있기 때문에 리튬 이온 전지의 대안이 고려되어야 할 필요가 있다.

많은 종류의 전지 중에서 소듐 이온 전지는 천연 자원의 풍부함과 저렴한 비용으로 주목을 받고 있다. 소듐은 리튬과 비슷한 화학적 특성을 공유하기 때문에 소듐 이온 전지의 기본 작동원리는 리튬 이온 전지와 동일하므로 리튬 이온 전지에 대한 연구성과들은 소듐 이온 전지의 전극 재료를 연구하는데 있어서 참고할 만한 훌륭한 예시이다. 그러나 적절한 음극재료에 대한 연구가 여전히 필요하기 때문에 소듐 이온 전지의 많은 연구들이 더 큰 용량을 발현 할 수 있는 새로운 소재를 개발하는 것에 중점을 두고 있다.

먼저 1장 서론에서는 리튬 이온 전지에 대하여 간략하게 소개한다. 리튬 이온 전지의 양극물질은 구조에 따라 세가지로 분류하여 설명하였고 음극물질은 반응메커니즘을 따라서 설명하였다. 뿐만 아니라 리튬 이온 전지의 대체하기 위한 소듐 이온 전지의 장점과 필요

성을 소개한다. 소듐 이온 전지는 리튬 이온 전지와 비슷한 원리로 작동하기 때문에 소듐 이온 전지의 양극물질과 음극물질에 대하여서도 소개를 한다.

2장에서는 헥테로 원자를 도핑한 그래핀의 전기화학적 특성에 대해 논의한다. 이 장에서는 소듐 이온 전지의 음극 물질로서 간단하고 경제적인 열처리 방법을 통해 높은 도핑 레벨과 무질서한 구조를 갖는 황으로 도핑된 그래핀을 제조하였다. 이 방법으로 합성한 황 도핑된 그래핀을 황이 도핑되는 않은 그래핀과 비교하여 소듐 이온 전지의 음극 물질로 사용하였을 때 훨씬 높은 가역용량과 우수한 사이클 안정성, 특히 우수한 속도특성을 보여주었다. 특히 장기 성능에서도 용량이 거의 감소하지 않는 뛰어난 전기화학적 특성을 보이는 이유는 높은 도핑 레벨로 인하여 늘어난 층간 거리(interlayer distance), 무질서한 구조와 더 많은 활성 사이트가 소듐 이온 저장에 도움을 주기 때문이다.

마지막 장에서는 소듐 이온 배터리의 음극 물질로서 볼 밀링(ball-milling) 방법을 통해 황화주석(II)/탄소 복합재(SnS/ composites)를 제조 하였다. 황화주석(II)/탄소 복합재의 전기 화학적 성능은 상용 SnS와 비교하였을 때 우수한 사이클 안정성과 특히 향상된 속도 특성을 나타내었다. 황화주석/탄소 복합재는 다양한 전류 속도에서 탁월한 용량 유지율을 나타내며 특히 높은 전류 밀도에서도 높은 용량을 제공하고 있다. 황화주석은 특히 복잡한 반응 메커니즘을 가지고 있

는데 그것은 전환반응(conversion reaction)과 합금반응(alloy reaction)으로 모두 반응을 하기 때문이다. 따라서 이러한 황화주석/탄소 복합재의 반응 메커니즘을 더 잘 이해하기 위해, 투과전자 현미경(ex-situ TEM), X선 흡수분광 분석 (X-ray absorption near edge structure) 및 X 선 회절 (X-ray diffraction)법을 사용하였다.

주요어: 소듐 이온 전지, 음극 물질, 황 도핑된 그래핀, 황화주석, 반응 메커니즘

학 번: 2014-30254